Contents lists available at ScienceDirect

Journal of Computational Physics

journal homepage: www.elsevier.com/locate/jcp

A Vlasov-Fokker-Planck-Landau code for the simulation of colliding supersonic dense plasma flows

Hanzhi Zhao[a,b], Suming Weng[a,b,*], Zhengming Sheng[a,b,c], Shi Jin[d], Jie Zhang[a,b,c]

[a] *Key Laboratory for Laser Plasmas (MoE), School of Physics and Astronomy, Shanghai Jiao Tong University, Shanghai,200240, China*
[b] *Collaborative Innovation Center of IFSA, Shanghai Jiao Tong University,Shanghai, 200240, China*
[c] *Tsung-Dao Lee Institute, Shanghai Jiao Tong University,Shanghai, 201210, China*
[d] *School of Mathematical Sciences, Institute of Natural Sciences, MOE-LSC, Shanghai Jiao Tong University, Shanghai 200240, China*

ARTICLE INFO

Article history:

Keywords:
Fokker–Planck-Landau equation,
Asymptotic-preserving scheme,
Fast spectral method,
Collisional plasma,
Supersonic flow

ABSTRACT

A Vlasov-Fokker-Planck-Landau (VFPL) code is developed for the study of colliding supersonic dense plasma flows, in which the VFPL equations for both electrons and ions are solved by the time splitting strategy in the two-dimensional Cartesian coordinate space and the two-dimensional velocity space (2D2V). To accurately handle two colliding supersonic plasma flows with their velocities even much higher than the thermal velocities of ions, the full Fokker-Planck-Landau operator is employed for the collision terms. Using advanced numerical methods such as the fast spectral method and the asymptotic-preserving scheme, the ion-ion and electron-electron collision terms can be properly solved with a relatively large time step so that both high accuracy and efficiency of the developed code can be achieved. Further, the quantum degeneracy effect due to the high density and relatively low initial temperature of the electrons is included in the model. In addition, both the energy and momentum conservation are well satisfied. The developed code provides a unique numerical tool to study the interactions between high-velocity high-density plasma flows, which may be encountered in some advanced schemes of inertial confinement fusion and laser-driven laboratory astrophysics experiments.

1. Introduction

Counterstreaming plasmas widely exist in many areas of research, such as laser-induced plasmas, astrophysical plasmas, and inertial confined fusion (ICF). Generally, they can be categorized into collisional and collisionless regimes. In the collisionless case, the direct interactions between charged particles are ignorable, and the particles are only affected by macroscopic electromagnetic fields associated with collective behaviors. Collisionless plasma flows are found in many astrophysical environments and laboratory experiments. In astrophysics and space physics,

*Corresponding author: E-mail: wengsuming@sjtu.edu.cn;

they are related to magnetospheric and heliospheric shocks, supernova remnants, pulsar winds and their nebula, active galactic nuclei, gammaray bursts, and clusters of galaxies shock waves, etc. [1, 2, 3]. In ICF, collisionless shock waves generated by high-energy laser play a pivotal role in the compression and heating of fuel targets. Usually, numerical simulations of the collisionless counterstreaming plasmas can be carried out with fluid codes, particle-in-cell (PIC) codes, or Vlasov codes [4, 5, 6]. In the collisional case, however, the strong exchange of energy and momentum are found between charged particles involving plasma jets, which are frequently encountered in laboratory [7, 8] and astrophysical environments [9, 10]. In such a scenario, kinetic effects are expected to be as important as fluid effects. For example, typical fluid simulations cannot well describe ion-ion and ion-electron interactions in the collision-dominant regime, where the ion (or electron) mean free path is comparable to the scale length of other physical processes. In order to accurately describe the plasma interpenetration and shock formation in this regime [11, 12, 13], kinetic effects both for ions and electrons should be taken into account. Based on the accurate kinetic equation, Vlasov-Fokker-Planck (VFP) simulations are particularly suitable for the simulation of counterstreaming plasmas in the collision-dominant regime [14, 15].

Previously, various VFP codes have been developed by many groups for different applications. For example, the VFP equation for electrons was solved to study the electron transport, plasma conductivity, magnetic field generation, and inverse bremsstrahlung, where the ions are considered to be in rest or as a cold fluid [16, 17, 18, 19, 20, 21, 22, 23, 24]. Some attention has also been paid to solving the VFP equation at the ion time scale for the problems related to shock waves in ICF implosion and fast ion transport. Larroche et al. developed an ion-kinetic model of the collisional plasma and extensively studied the ICF implosion through their multi-species VFP simulations [25, 26, 27, 28, 29]. And a multiple-moving velocity-space adaptivity strategy for VFP equation was proposed by Taitano et al. [30, 31], where the velocity grid is normalized and shifted in terms of the thermal speed and the drift velocity, respectively. And due to the short electron collision time, the hydrodynamic model is usually applied for the electrons in these kinetic studies of ion dynamics.

For the Fokker-Planck equation, there are two widely used forms of collision operator in plasma physics. The Fokker-Planck-Landau (FPL) operator is an integro-differential equation form, while the Rosenbluth-Fokker-Planck (RFP) is expressed as a differential equation, where the diffusion and advection coefficients are solved by Poisson equations. Although these two forms of the operator are equivalent, in numerical schemes, it is generally accepted that FPL has better conservation properties, while RFP benefits from faster solving speed. For the VFP simulation introduced above, many codes adopt the RFP operator for fast implicit implementation, and some choose the FPL [32, 33]. For RFP equation, the method of the Legendre expansion for Rosenbluth potentials is often used to reduce the high-dimensional problem to a one-dimensional problem, which assumes that the distribution function is mainly isotropic and the anisotropic parts are small perturbation terms.

However, in some advanced ignition schemes of the ICF, such as impact ignition and double cone ignition, the colliding between dense highly supersonic plasma flows will be involved. In the impact ignition, a part of the fuel is accelerated to a super-high velocity and then it collides with a precompressed main fuel. To convert enough kinetic energy into thermal energy, the impactor velocity needs to be as high as 1100-1500 km/s [34, 35, 36, 37]. Similarly, the double-cone ignition scheme involves a head-on collision between two precompressed targets, where their velocities can reach hundreds of km/s [38]. In such conditions, the distribution function of the charged particles in phase space is far away from the Maxwellian distribution for the equilibrium state, as shown in Figs. 1(a) and 1(b). For such a high-Mach-number plasma, the assumption of small deviations from the Maxwellian distribution is no longer valid. As a result, the higher order terms of Legendre expansion of the distribution function will be even larger than the lower order terms in some velocity regions, as shown in Fig. 1(c), for example. An alternative approach to this problem is to adopt the co-moving frame in which the plasma is stationary [39]. But this approach does not work well for two colliding supersonic dense plasma flows. In this case, it is hard to define a co-moving frame since the distribution function has two separated parts in the phase space and these two parts quickly evolve due to their strong interaction. Some more costly strategies need to be employed [40, 41] to overcome this difficulty, and recently, Taitano et al. developed an implicit algorithm for RFP equation [42, 43], and this scheme is not limited by the above dilemma. Their one-dimensional code address scenarios when the drift velocity is much greater than the thermal velocity as well as adaptivity in the configuration-space grid [30].

On the other hand, the applications of FPL equations also have faced serious challenges. Due to the integro-differential nature, achieving a fully implicit scheme is difficult, and the computational complexity prevents it from being implemented. Fortunately, some fast schemes have been developed to reduce computational complexity [44, 45, 46], and the asymptotic-preserving (AP) methods for FPL equation have been proposed by Jin et al. to accelerate the

computing speed by penalization techniques [47, 48]. These advanced numerical schemes allow one to achieve high accuracy and computational efficiency for specific physical problems. Meanwhile, the numerical methods preserve good energy conservation and are easily scalable to higher dimensions. For the reasons given above, we choose the FPL operator to handle colliding supersonic dense plasma. Furthermore, the quantum degeneracy effect of the electrons in dense plasmas may impact the collision process of plasma flows [49, 50], which has not been extensively studied in VFP previously. Brown et al. expanded a degenerate form of the Fokker–Planck collision operator [51], and this modified Fokker–Planck collision operator was employed to study the electron transport [52]. Also, the fast method has been developed for the quantum Fokker-Planck-Landau (qFPL) equation [53]. Previous studies have shown that the degenerate effects have a significant effect on dense plasma. Thus the quantum electrons collision also needs to be considered in some ICF scenarios.

In this paper, we develop the first, to the best of our knowledge, two-dimensional multi-species code dedicated exclusively to the studies of colliding supersonic dense plasma flows, where both the electrons and ions are treated fully kinetically and accurately. This code solves the Vlasov-Fokker-Planck-Landau (VFPL) equations for the electrons and ions by the splitting strategy in two-dimensional Cartesian coordinate space and two-dimensional velocity space (2D2V). With the asymptotic-preserving scheme and the fast spectral method, this code has the capability of being able to model the interaction between supersonic dense plasma flows from the kinetic to fluid regimes and is not limited by the strong anisotropy in the distribution. Specifically, the AP scheme allows one to use coarse meshes and large time steps and thus achieve both high accuracy and computational efficiency for our physical problem. In addition, the full qFPL treatment for degenerate electrons and self-consistent ion-electron collisions are also considered in our code. This code provides a unique numerical tool with high computational efficiency and good accuracy to study counterstreaming dense plasma with high drift velocity.

The rest of the paper is organized as follows. Section 2 introduces the basic equations to be solved. Section 3 gives the numerical schemes for solving the VFPL. In particular, the fast spectral method for the Fokker-Planck-Landau collision operator [44] and the asymptotic-preserving scheme for the collision equation [47, 48] are applied. Several numerical examples for the interaction between two counterstreaming dense plasma flows are presented to test the codes in Sec 4. Finally, the discussion and conclusions are given in Sec 5.

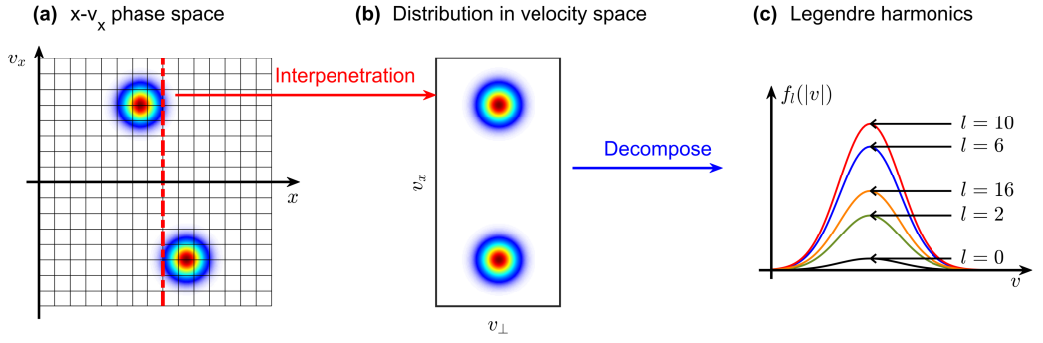

Fig. 1. The schematic diagram of the counterstreaming plasma blocks. (a) The distribution function of ions in x-v_x phase space. (b) The distribution function in the velocity space on the interpenetration surface (red dashed line in (a)). (c) The decomposed distributions in Legendre harmonics $f_l(|v|)$ of order l=0, 2, 6, 10, 16.

2. Basic Equations and Variable Normalization

The distribution functions of the ions and electrons $f_{\alpha,e}(\mathbf{x}, \mathbf{v}, t)$ are governed by the following VFP equations:

$$\begin{aligned}
&\frac{\partial f_\alpha}{\partial t} + \mathbf{v}\frac{\partial f_\alpha}{\partial \mathbf{x}} + \frac{m_\alpha \mathbf{E}}{Z_\alpha e}\frac{\partial f_\alpha}{\partial \mathbf{v}} = \sum_\beta C_{\alpha\beta}\left(f_\alpha, f_\beta\right) + C_{\alpha e}\left(f_\alpha\right), \\
&\frac{\partial f_e}{\partial t} + \mathbf{v}\frac{\partial f_e}{\partial \mathbf{x}} - \frac{m_e \mathbf{E}}{e}\frac{\partial f_e}{\partial \mathbf{v}} = C_{ee}\left(f_e\right) + \sum_\alpha C_{e\alpha}\left(f_e\right),
\end{aligned} \tag{1}$$

where the subscripts α and β represent the particle species for the ions, while the subscript e represents the electrons. The collision term between the species α and β is denoted by $C_{\alpha\beta}$, whereas C_{ee} represents the collision term between the electrons. $C_{e\alpha}$ and $C_{\alpha e}$ represent the electron-ion collision and ion-electron collision, respectively. Additionally, the variables $\mathbf{x}$ and $\mathbf{v}$ are the spatial and velocity coordinates, respectively. Z_α and m_α are the charge number and mass for the ion species α, respectively. Furthermore, e is the unit charge, and $\mathbf{E}$ on the left side of the equation is the electric field governed by the Poisson equation:

$$\nabla \cdot \mathbf{E} = 4\pi e\left(\sum_a Z_\alpha n_\alpha - n_e\right). \tag{2}$$

Taking different order moments of the velocity distribution function, the density n_α, flow velocity $\mathbf{u}_\alpha$, internal energy e_α and energy ε_α of the particles α are given by:

$$\begin{aligned} n_\alpha &= \int f_\alpha(\mathbf{v})\, d\mathbf{v}, \\ n_\alpha \mathbf{u}_\alpha &= \int f_\alpha(\mathbf{v})\, \mathbf{v} d\mathbf{v}, \\ n_\alpha e_\alpha &= \frac{m_\alpha}{2}\int f_\alpha(\mathbf{v})\, |\mathbf{v}-\mathbf{u}|^2 d\mathbf{v}, \\ n_\alpha \varepsilon_\alpha &= \int f_\alpha(\mathbf{v})\, \mathbf{v}^2 d\mathbf{v}. \end{aligned} \tag{3}$$

For the collision term between the ions in Eq. (1), it can be described by the Fokker-Planck-Landau (FPL) collision operator:

$$C_{\alpha\beta}\left(f_\alpha, f_\beta\right) = -\frac{2\pi \ln_{\alpha\beta} Z_\alpha^2 Z_\beta^2 e^4}{m_\alpha}\frac{\partial}{\partial v_\delta}\int\left\{\frac{f_\alpha(\mathbf{v})}{m_\beta}\frac{\partial f_\beta(\mathbf{v}')}{\partial v'_\gamma} - \frac{f_\beta(\mathbf{v}')}{m_\alpha}\frac{\partial f_\alpha(\mathbf{v})}{\partial v_\gamma}\right\}U_{\delta\gamma} d\mathbf{v}' \tag{4}$$

where $\mathbf{U}$ is a nonnegative and symmetric matrix of the form

$$U_{\alpha\beta} = \frac{1}{|\mathbf{v}-\mathbf{v}'|^3}\left\{\left|\mathbf{v}-\mathbf{v}'\right|^2\delta_{\alpha\beta} - \left(v_\alpha - v'_\alpha\right)\left(v_\beta - v'_\beta\right)\right\}. \tag{5}$$

The FPL collision operator has the properties of conserving mass, momentum, and energy:

$$\int C_{\alpha\beta} d\mathbf{v} = 0, \quad \sum_{\alpha,\beta} m_\alpha \int C_{\alpha\beta}\mathbf{v} d\mathbf{v} = 0, \quad \sum_{\alpha,\beta} m_\alpha \int C_{\alpha\beta}\mathbf{v}^2 d\mathbf{v} = 0. \tag{6}$$

Meanwhile, it satisfies Boltzmann's H theorem:

$$-\int C_{\alpha\alpha}\log\left(f_\alpha(\mathbf{v})\right) d\mathbf{v} \geq 0. \tag{7}$$

Moreover, the equilibrium distribution function is the local Maxwellian distribution function

$$f_M(\mathbf{v}) = \frac{n}{(2\pi T)^{d/2}}\exp\left(-\frac{|\mathbf{v}-\mathbf{u}|^2}{2T}\right), \tag{8}$$

and d is the dimension number of the velocity space. The Coulomb logarithm in Eq. (4) is expressed in the form

$$\ln_{\alpha\beta} = \frac{1}{2}\ln\left(1 + b_{\max}^2/b_{\min}^2\right), \tag{9}$$

where the upper b_{max} and lower b_{min} are cutoffs described by Brysk et al. [54]. Since the difference between the respective Coulomb logarithm $\ln_{ee}$ and $\ln_{ei}$ for the electrons and the ions is only noticeable at extremely high density and low temperature (i.e. $10^{27}\mathrm{cm}^{-3}$ and 10eV), the same value is used for them in our simulation.

If we assume that the self-collision term $C_{\alpha\alpha}$ is the leading term in the VFP equation for the ions, the strong self-collisions will ensure that the distribution function is nearly an equilibrium distribution. With the Maxwellian distribution assumption, the different order moments of the VFP equation yield the following multispecies fluid equations:

$$\begin{aligned}
&\frac{\partial n_\alpha}{\partial t} + \nabla_x \cdot (n_\alpha \mathbf{u}_\alpha) = 0, \\
&m_\alpha n_\alpha \left(\frac{\partial}{\partial t} + \mathbf{u}_\alpha \cdot \nabla_x \right) u_{\alpha,\gamma} + \frac{\partial n_\alpha T_\alpha}{\partial x_\gamma} - Z_\alpha e n_\alpha = \sum_\beta R_{\alpha\beta,\gamma} + R_{e\alpha,\gamma}, \\
&\frac{3}{2} n_\alpha \left(\frac{\partial}{\partial t} + \mathbf{u}_\alpha \cdot \nabla_x \right) T_\alpha + n_\alpha T_\alpha \nabla_x \cdot \mathbf{u}_\alpha + \nabla_x \cdot \mathbf{q}_\alpha = \sum_\beta Q_{\alpha\beta} + Q_{e\alpha},
\end{aligned} \tag{10}$$

where $\mathbf{q}_\alpha$ is the heat flux, and the Spitzer-Härm heat flux is often used. $\mathbf{R}_{\alpha\beta}$ and $Q_{\alpha\beta}$ are the friction force and heat terms between particles α and β, respectively. It is worth pointing out that this multifluid model requires that the mean free path $\lambda_{\alpha\alpha}$ for the self-collisions is not only much smaller than the scale length $L = |f_\alpha / \nabla f_\alpha|$, but also much smaller than the mean free path $\lambda_{\alpha\beta}$ for the collisions between the different ion species. Later we will show that the second requirement may be not satisfied in some tests, in which the multifluid model fails.

For the electron-electron collision term, the full collision model has been implemented in our model, including quantum statistical effects. For the degenerate electrons in a dense plasma, the quantum Fokker-Planck-Landau (qFPL) operator is given by [51]

$$C_{ee}(f_e) = -\frac{2\pi L n_{ee} e^4}{m_e^2} \frac{\partial}{\partial v_\delta} \int \left\{ f_e(\mathbf{v}) \left(1 - \theta_e f_e(\mathbf{v})\right) \frac{\partial f_e(\mathbf{v}')}{\partial v'_\gamma} - f_e(\mathbf{v}') \left(1 - \theta_e f_e(\mathbf{v}')\right) \frac{\partial f_e(\mathbf{v})}{\partial v_\gamma} \right\} U_{\delta\gamma} d\mathbf{v}', \tag{11}$$

where $\theta_e = (2\pi\hbar)^d / 2$, so that $d\mathbf{v}/\theta_e$ represents the number of available states in the phase space. This expression reduces to the classical collision limit when $|\theta_e f_e(\mathbf{v})| \ll 1$. The qFPL operator also satisfies the conservation and H theorem. With the qFPL operator, the equilibrium states take the Fermi-Dirac distribution

$$f_{FD}(\mathbf{v}) = \frac{1}{\theta_e} \left[1 + \exp\left(\frac{\mu - (\mathbf{v} - \mathbf{u})^2 / 2}{T} \right) \right]^{-1}, \tag{12}$$

where μ is the electrostatic potential and $\mathbf{u}$ is the flow velocity. It is usually defined T/E_F as a parameter to characterize the degree of quantum degeneracy, with the Fermi temperature $\mathrm{E}_F = \hbar^2 / 2 m_e (3\pi^2 n_e)^{2/3}$. In dense and cold plasmas, the quantum degeneracy effect of electrons cannot be neglected. The degree of quantum degeneracy influences the collisional transfer rates. For instance, the electron-ion relaxation time in the quantum degeneracy regime is modified as [49]

$$\frac{1}{\tau_{ei}} = \frac{(4\pi)^2 Z e^4 \ln_{ei} m_e n_i}{3\theta n_e} \frac{1}{1 + e^{-\mu/T}}, \tag{13}$$

when $m_e/m_i \ll \mathrm{T_e}/\mathrm{T_i}$ that is well satisfied in most physical situations. According to Eq. (13), the degeneracy effect becomes obvious when the electrostatic potential energy is comparable to the electron thermal energy. Correspondingly, the modified relaxation time is longer than its classical limit. For counterstreaming plasmas, the quantum effect may affect the energy exchange process between the electrons and the ions.

The ion-ion collision term and degenerate electron-electron collision term will be solved by the fast spectral method as described in the next section. However, the ion-electron collision term is generally hard to be solved directly due to the sizeable ion-to-electron mass ratio, which makes the fast spectral method ineffective. Therefore a simplified operator for the ion-electron collisions should be considered. Following Braginskii [55], one can expand the matrix $U_{\alpha\beta}$ in powers of the ratio of the ion $\mathbf{v}$ velocity to electron velocity $\mathbf{v}'$, and only retain the first term

$$U_{\alpha\beta} = \frac{1}{|\mathbf{v}'|^3} \left\{ |\mathbf{v}'|^2 \delta_{\alpha\beta} - v'_\alpha v'_\beta \right\}, \tag{14}$$

which results from the fact that normally the electron velocities are much larger than the ion velocities. Further, we assume that the electron distribution is in an approximate equilibrium state, and a slight distortion in the electron

distribution does not affect the value of the collision term. As a result, the ion-electron collision term takes the following approximate form:

$$C_{ie}(f_\alpha) = \frac{m_e n_e}{m_\alpha n_\alpha}\frac{1}{\tau_{ei}}\frac{\partial}{\partial v_\beta}\left(\left(v_\beta - u_{e,\beta}\right) f_\alpha + \frac{T_e}{m_\alpha}\frac{\partial f_\alpha(\mathbf{v})}{\partial v_\beta}\right). \tag{15}$$

For the ions, the above collision operator can capture the exchange of momentum and energy between the electrons and ions.

For the electrons, the momentum and energy gained (or lost) from the electron-ion collisions are calculated according to the momentum and energy conservation, and a simplified electron-ion collision is adopted in our code. Since the relaxation time of the electrons is far shorter than that of the ions, many simulation models usually assume that the electron distribution has reached a quasi-steady state when considering the dynamic of the ions. To estimate the electron kinetic effects, we take a simplified description for the electron distribution with the Krook model (or BGK model) [56] as follows

$$C_{ei}(f_e) = -\frac{1}{\tau_{ei}}\left(f_e - \bar{f}\right), \tag{16}$$

where $\bar{f}$ is the local Maxwellian distribution with the density, momentum, and temperature calculated by the electron distribution function f_e. The Krook model is the most straightforward and most numerically economical. Meanwhile, it maintains the main properties of Coulomb collisions and has the same fluid (compressible) Euler limit as the relaxation time goes to zero. Moreover, its validity and improvement have been studied for many years [57, 58].

In the following, we present our numerical schemes to solve the equations given above. We adopt normalized units with the characteristic temperature T_0 and number density n_0. The thermal velocity corresponding to the temperature is defined as $v_0 = (2T_0 m_p)^{1/2}$ with m_p the proton mass. Time is normalized to the collision time $t_0 = 3m_p^2 v_0^3 \big/ 16\pi^{1/2} n_0 e^4$, and length is normalized to the mean free path $\lambda_0 = v_0 t_0$. And the distribution function f is normalized to n_0/v_0^d. The physical quantities for time, length, velocity, density, ion mass, temperature, and electric field are normalized as follows:

$$\begin{aligned} &t \to t/t_0,\ \mathbf{x} \to \mathbf{x}/\lambda_0,\ v \to v/v_0,\ n_a \to n_a/n_0, \\ &m_a \to m_a \big/ m_p,\ T_a \to T_a \big/ m_p v_0^2,\ \mathbf{E} \to t_0 e\mathbf{E} \big/ m_p v_0. \end{aligned} \tag{17}$$

The full set of equations using the above normalisations is given by

$$\begin{aligned} &\frac{\partial f_\alpha}{\partial t} + \mathbf{v}\frac{\partial f_\alpha}{\partial \mathbf{x}} + \frac{A_\alpha \mathbf{E}}{Z_\alpha}\frac{\partial f_\alpha}{\partial \mathbf{v}} = \sum_\beta C_{\alpha\beta}\left(f_\alpha, f_\beta\right) + C_{\alpha e}(f_\alpha), \\ &\frac{\partial f_e}{\partial t} + \mathbf{v}\frac{\partial f_e}{\partial \mathbf{x}} - \mathbf{E}\frac{\partial f_e}{\partial \mathbf{v}} = C_{ee}(f_e) + \sum_\alpha C_{e\alpha}(f_e), \\ &\nabla \cdot \mathbf{E} = \frac{4\pi n_0 e^2 t_0^2}{m_p}\left(\sum_a Z_\alpha n_\alpha - n_e\right), \end{aligned} \tag{18}$$

and the collision terms are given by:

$$\begin{aligned} C_{\alpha\beta}\left(f_\alpha, f_\beta\right) &= -\frac{3\sqrt{\pi}\ln_{\alpha\beta} Z_\alpha^2 Z_\beta^2}{8A_\alpha^2}\frac{\partial}{\partial v_\delta}\int\left\{\frac{A_\alpha}{A_\beta} f_\alpha(\mathbf{v})\frac{\partial f_\beta(\mathbf{v}')}{\partial v'_\gamma} - f_\beta(\mathbf{v}')\frac{\partial f_\alpha(\mathbf{v})}{\partial v_\gamma}\right\} U_{\delta\gamma} d\mathbf{v}', \\ C_{ee}(f_e) &= -\frac{3\sqrt{\pi}\ln_{ee}\mu_0^2}{8}\frac{\partial}{\partial v_\delta}\int\left\{f_e(\mathbf{v})\left(1 - \theta_e f_e(\mathbf{v})\right)\frac{\partial f_e(\mathbf{v}')}{\partial v'_\gamma} - f_e(\mathbf{v}')\left(1 - \theta_e f_e(\mathbf{v}')\right)\frac{\partial f_e(\mathbf{v})}{\partial v_\gamma}\right\} U_{\delta\gamma} d\mathbf{v}', \\ C_{\alpha e}(f_\alpha) &= \frac{n_e\mu_0}{A_\alpha n_\alpha}\frac{1}{\tau_{e\alpha}}\frac{\partial}{\partial v_\beta}\left(\left(v_\beta - u_{e,\beta}\right) f_\alpha + \frac{T_e}{A_\alpha}\frac{\partial f_\alpha(\mathbf{v})}{\partial v_\beta}\right), \\ C_{e\alpha}(f_e) &= -\frac{1}{\tau_{e\alpha}}\left(f_e - \bar{f}\right), \end{aligned}$$

where $A_\alpha = m_a/m_p$ and $\mu_0 = m_p/m_e$.

3. Numerical schemes for time integration and the Vlasov equation

3.1. Time Integration

We adopt the time-splitting scheme to solve the VFP equation [59], which was first invented by Cheng and Knorr [60] and is now widely utilized to solve multidimensional partial-differential equations (PDEs). The split scheme requires less memory space and allows a relatively large time step than the unsplit methods. For the VFP equation, we decompose VFP equations into several one-dimensional advection equations and collision operators, then advance the distribution function from t^n to t^{n+1} given by

$$\begin{aligned} &f\left(\mathbf{x},\mathbf{v},t^{n+1}\right)=T\left(\Delta t/2\right)S\left(\Delta t\right)T\left(\Delta t/2\right)f\left(\mathbf{x},\mathbf{v},t^{n}\right), \\ &T\left(\Delta t\right)=T_x\left(\Delta t/2\right)T_y\left(\Delta t/2\right)T_{v_x}\left(\Delta t\right)T_{v_y}\left(\Delta t\right)T_x\left(\Delta t/2\right)T_y\left(\Delta t/2\right), \end{aligned} \tag{19}$$

where $T_x\left(\Delta t/2\right)$and $T_y\left(\Delta t/2\right)$ denote the advection operators with a half time step $\Delta t/2$ along the x and y directions, respectively. $T_{v_x}\left(\Delta t\right)$ and $T_{v_y}\left(\Delta t\right)$ denote the advection operators with time step Δt along the v_x and v_y direction, respectively, and $S\left(\Delta t\right)$ is the collision operator with time step Δt. Here we use Strang's splitting to get a second-order accuracy in the time splitting scheme. The Poisson equation is solved to update the electric field before the execution of advection operators T_{v_x} and T_{v_y} in the velocity space. Here the time step for updating the distribution function is chosen to be

$$\Delta t=\min\left(\Delta t_s,\Delta t_v,\Delta t_c\right), \tag{20}$$

where Δt_c, Δt_s, and Δt_v are the time steps for the collision operator, and the advection equations in coordinate and velocity spaces, respectively. Usually, the collision operators determine the restriction condition or the time step for a dense plasma. The Courant–Friedrichs–Lewy (CFL) condition for the Vlasov part satisfies $\Delta t_s < C\Delta x/v$ and $\Delta t_v < C\Delta v/\left(A_\alpha E/Z_\alpha\right)$, while the explicit schemes of the collision operators suffer from the constraint $\Delta t_c < C\tau_e\Delta v^2$ or $\Delta t_c < C\tau_i\Delta v^2$, where the characteristic electron and ion collision times can be written in the form:

$$\tau_e=\frac{3\sqrt{m_e}T_e^{3/2}}{4\sqrt{2\pi}\ln_{ei}e^4Z^2n_i},\quad \tau_i=\frac{3\sqrt{m_i}T_i^{3/2}}{4\sqrt{\pi}\ln_{ii}e^4Z^4n_i}. \tag{21}$$

The hydrodynamic time scale is longer than the collisional processes in our case as shown in the following.

3.2. The Vlasov equation

For the Vlasov equation, the primary step is to solve the advection equation:

$$\frac{\partial f(x,t)}{\partial t}+v\frac{\partial f(x,t)}{\partial x}=0. \tag{22}$$

There are numerous algorithms to solve this advection equation, and we adopt the semi-Lagrangian time integration scheme [61]. The semi-Lagrangian scheme guarantees mass conservation strictly [60, 62] and has been extensively studied and widely used in the Vlasov equation in the past decades. According to this scheme, given the value of function f at the i-th mesh, the new value at the next time step is given by

$$f(x_i,t_n+\Delta t)=f(X(t_n,t_n+\Delta t,x_i),t_n), \tag{23}$$

where X is the position of the characteristic curve. We denote by f_i^n the averaged value of the distribution function over the i-th grid at time t^n, then the new distribution at the next time step is

$$f_i^{n+1}=f_i^n+\Phi_{i-1/2}^n-\Phi_{i+1/2}^n, \tag{24}$$

where the numerical flux is

$$\Phi_{i\pm1/2}^n=\frac{1}{\Delta x}\int_{X(t_n,t_n+\Delta t,x_i)}^{x_i\pm\Delta x/2}f(x,t_n)dx. \tag{25}$$

The essential step for the semi-Lagrangian method is to interpolate the distribution function [62]. The most used scheme is the positive flux conservation scheme (PFC) proposed by Filbet et al. [63]. Here, we adopt the high-order monotonicity- and positivity-preserving schemes introduced by Tanaka et al. [64]. This method is based on the conservative semi-Lagrangian scheme (CSL) [65] with the monotonicity-preserving constraint and the positivity-preserving limiter to ensure the positivity and monotonicity of the numerical solution. The schemes have high-order accuracy, and the details of each step can be found in Ref. [64].

The Poisson equation is solved numerically before the iteration of the distribution function. Because the cost of solving the Poisson equation is much less than calculating the collision terms, we use the multigrid method to update the electric field directly.

3.3. Method to deal with the ion collision term

3.3.1. Numerical scheme for the FPL equation

The ion-ion collision term is described by the Landau collision operator in Eq. (4) shown above. Due to the multidimensional nature of the distribution function and the threefold integral of the Landau operator, the numerical solution of the FPL equation is difficult and expensive. There are several numerical schemes of the full Fokker-Planck equation [19]. The RFP collision operator is often utilized in the numerical investigation implicitly [18, 40, 66]. Several studies considered a simpler diffusive Fokker-Planck model [67] or took the polar or cylindrical coordinates [12, 41, 68]. In order to reduce computational complexity and cost, some fast algorithms have been proposed for FPL operator, such as multipole expansions [46], and multigrid techniques [45, 69]. In our code, we adopt a fast algorithm with a reduced computational cost while preserving the accuracy of the Fokker-Planck operator by using the fast spectral method for the FPL collision operator [44], and the asymptotic-preserving scheme to solve the collision equation [47].

The fast spectral method is based on a Fourier spectral approximation of the distribution function. It allows us to reduce the computational cost from $O(N^2)$ to $O(N \log_2 N)$, where N is the total number of grids in the velocity space. Further details of the fast spectral method can be found in Ref. [44]. Here we extend this method for the collisions between different particle species. The main idea of this method is to approximate the distribution function by the truncated Fourier series:

$$f^N(\mathbf{v}) = \sum_{\mathbf{k}=-N}^{N} \hat{f}_{\mathbf{k}} e^{i\mathbf{k}\cdot\mathbf{v}}, \tag{26}$$

where $\mathbf{k}$ donates the vector of integers and N is the number of half modes. Then substituting the series into Eq. (4), we obtain the collision operator for each Fourier mode $\hat{f}_{\mathbf{k}}$ with a simple change of variable:

$$C_{\alpha\beta}^N\left(f_\alpha^N, f_\beta^N\right) = \left(\frac{2\pi L n_{\alpha\beta} e_\alpha^2 e_\beta^2}{m_\alpha^2}\right) \sum_{\mathbf{k}=-N}^{N} \hat{C}_{\alpha\beta,\mathbf{k}} e^{i\mathbf{k}\cdot\mathbf{v}}, \tag{27}$$

$$\hat{C}_{\alpha\beta,\mathbf{k}} = \sum_{\mathbf{m}=-N}^{N} \hat{f}_{\alpha,\mathbf{k}-\mathbf{m}} \hat{f}_{\beta,\mathbf{m}} \hat{\beta}_L\left(\mathbf{k}-\mathbf{m}, \mathbf{m}\right).$$

The kernel integral $\hat{\beta}_L\left(\mathbf{k}, \mathbf{m}\right)$ in Eq. (27) is given by

$$\hat{\beta}_L\left(\mathbf{k}, \mathbf{m}\right) = \int_{B(0,\pi)} |g|^{-1} \left[\left(\mathbf{k}+\mathbf{m}\right)\left(\mathbf{k}-\mathbf{m}\right) - \frac{m_\alpha}{m_\beta} |g|^{-2} \left(\mathbf{k}+\mathbf{m}\right)\cdot\mathbf{g}\left(\mathbf{k}-\mathbf{m}\right)\cdot\mathbf{g}\right] e^{i\mathbf{g}\cdot\mathbf{m}} d\mathbf{g}, \tag{28}$$

where the integration limits $B(0,\pi)$ are the ball of a radius π in the phase space. The kernels $\hat{\beta}_L\left(\mathbf{k}, \mathbf{m}\right)$ are completely independent of the distribution function, thus one only needs to calculate them accurately for one time and can acquire their values directly from the storage in the next time steps.

To further reduce the computational cost, we can split $\hat{\beta}_L(\mathbf{k},\mathbf{m})$ and rewrite Eq. (27) as

$$\begin{aligned}\hat{C}_{\alpha\beta,\mathbf{k}} = & \sum_{\mathbf{m}=-N}^{N} \hat{f}_{\alpha,\mathbf{k}-\mathbf{m}}\hat{f}_{\beta,\mathbf{m}} F(\mathbf{m})(\mathbf{k}-\mathbf{m})^2 \\ & - \sum_{\mathbf{m}=-N}^{N} \hat{f}_{\alpha,\mathbf{k}-\mathbf{m}}\hat{f}_{\beta,\mathbf{m}} B_L(\mathbf{m},\mathbf{m}) - \sum_{\mathbf{m}=-N}^{N}\sum_{p,q=1}^{d} \hat{f}_{\alpha,\mathbf{k}-\mathbf{m}}\hat{f}_{\beta,\mathbf{m}}\left(k_p-m_p\right)\left(k_q-m_q\right) I_{pq}(\mathbf{m}) \\ & + \left(1-\frac{m_\alpha}{m_\beta}\right)\sum_{\mathbf{m}=-N}^{N}\sum_{p=1}^{d} \hat{f}_{\alpha,\mathbf{k}-\mathbf{m}}\hat{f}_{\beta,\mathbf{m}}\left(k_p-m_p\right) G_p(\mathbf{m},\mathbf{m}),\end{aligned} \tag{29}$$

where

$$\begin{aligned} F(\mathbf{m}) &= \int_{B(0,\pi)} |g|^{-1} e^{i\mathbf{g}\cdot\mathbf{m}} d\mathbf{g}, \\ I_{pq}(\mathbf{m}) &= \int_{B(0,\pi)} |g|^{-3} g_p g_q e^{i\mathbf{g}\cdot\mathbf{m}} d\mathbf{g}, \\ B_L(\mathbf{k},\mathbf{m}) &= \mathbf{k}^2 F(\mathbf{m}) - \sum_{p,q=1}^{d} k_p k_q I_{pq}(\mathbf{m}), \\ G_p(\mathbf{k},\mathbf{m}) &= \mathbf{k}^2 F(\mathbf{m}) - \sum_{q=1}^{d} k_q I_{pq}(\mathbf{m}), \end{aligned}$$

When the mass of particle species α and β are the same, the collision term returns to the form given in Ref. [44]. For the accurate computation of kernel integrals, one may refer to Ref. [70]. Finally, it is straightforward to transform the summation through the convolution theorem, and we can solve the FPL equation in $O(N\log_2 N)$ using the Fast Fourier Transform. In addition to its high precision and low cost, another advantage of the FSM is its good expansibility for multi-dimension cases. This is a superiority over solving the Poisson equation of the Rosenbluth potentials, which is difficult to be extended to the three-dimensional velocity space.

In splitting schemes, the time step is typically limited by collision terms. Although the collision terms can be calculated accurately using implicit schemes, they are usually expensive and complicated. On the other hand, for an explicit scheme, the time step is restricted by the collision time, which affects the application of the code for highly dense plasmas. To overcome the stability constraint for the explicit scheme, Filber and Jin proposed an asymptotic-preserving (AP) scheme for the FPL equation [47], which is adopted in our code. Using the AP scheme, the collision equation is discretized in time as

$$\frac{f^{n+1}-f^n}{\Delta t} = C(f^n) - \zeta P^n(f^n) + \zeta P^{n+1}\left(f^{n+1}\right), \tag{30}$$

where the penalization operator is given by

$$P(f) = \nabla_{\mathbf{v}}\cdot\left(f_M \nabla_{\mathbf{v}}\left(\frac{f}{f_M}\right)\right). \tag{31}$$

Here ζ is a constant related to the distribution function, which is best chosen as

$$\begin{aligned} \zeta &= \left(2+\sqrt{2}\right)\max_{\mathbf{v}} \lambda\left(\mathbf{D}_A(f)\right), \\ \mathbf{D}_A(\mathbf{v}) &= \int \mathbf{U}(\mathbf{v}-\mathbf{v}') f(\mathbf{v}')\, d\mathbf{v}', \end{aligned} \tag{32}$$

where $\lambda(\mathbf{D}_A)$ is the spectral radius of the matrix $\mathbf{D_A}$. The AP scheme penalizes the nonlinear collision operator by a penalization operator $P(f)$ and the stiffness of the FPL operator is overcome by solving the penalization operator implicitly. Here the operator $P(f)$ is a linear operator whose implicit solution can be easily achieved, while the full FPL operator $C(f)$ can be explicitly calculated by the efficient FSM. The AP schemes are able to handle multiple

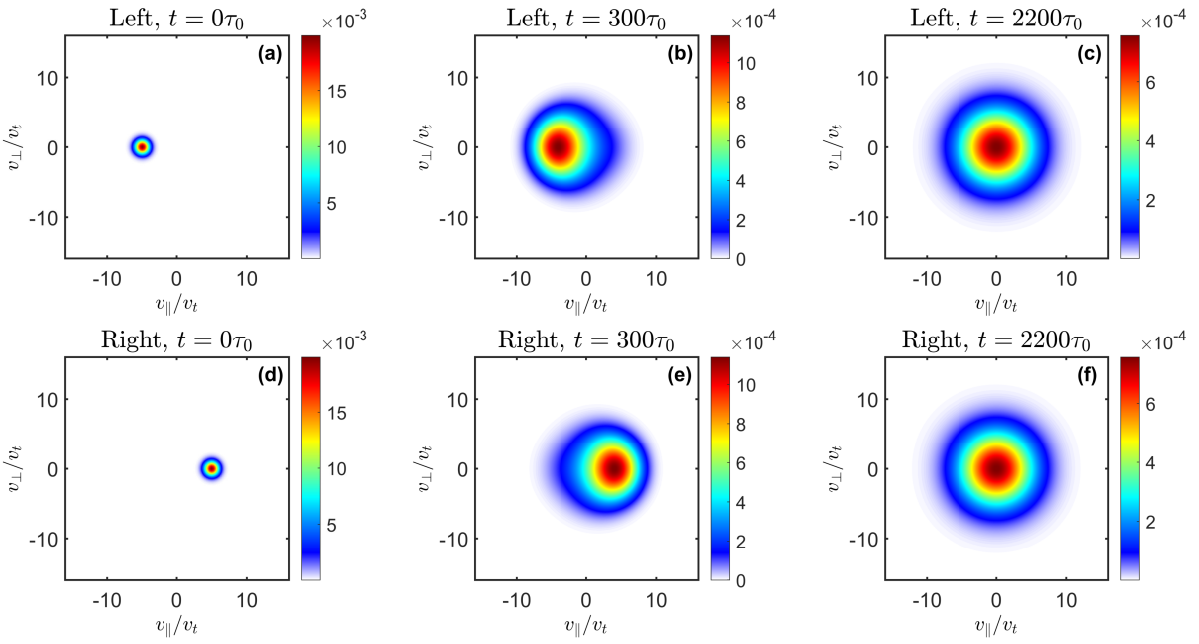

Fig. 2. Evolution of the ion distribution functions for two colliding plasma flows with identical ion species. The top row is for the ion distribution with a negative initial drift velocity, and the bottom row is for another ion distribution. Axis $v_\parallel$ represents the velocity parallel to the flow, while $v_\perp$ perpendicular to the drift velocity.

scales from kinetic regimes to fluid regime, efficiently [48], and has been developed for many years [71, 72, 73]. Specifically, this scheme allows one to use coarse meshes and large time-steps to capture the macroscopic behavior even if the small physical scales are under-resolved. In addition, the scheme we adopted preserves the mass strictly in time, while the conservation of momentum and energy is controlled by the spectral accuracy, except for the projection error [32]. By selecting the appropriate grids for different physical problems, acceptable numerical errors can be achieved. Typically, we set the normalized units according to the initial ion density and temperature, with a time step $t = 0.01t_0$ to balance the computational cost and accuracy.

3.3.2. Numerical test of the FPL model

To validate the numerical scheme given above, we perform some test simulations for the ion-ion collisions between two colliding plasma flows, in which the ion species of two colliding plasma flows can be either identical or different.

Figure 2 shows the snapshots of the distribution function at different times to illustrate the collisional slowing-down process between the counterstreaming ions. The initial relative drift velocity u between the two distribution functions is set as ten times the thermal velocity of the ions v_t to test the ability to simulate supersonic plasma flows and their initial distribution functions are assumed to be drift-Maxwellian as shown in Fig. 2(a) and Fig. 2(d), with the same initial number density and temperature. The simulation depicts the isotropization and thermalization process of two particle distributions. Under the influence of the collisions between counterstreaming ions, the two distribution functions, which initially are far-separated from each other in the phase space, approach each other and finally both of them stop at around $\mathbf{v} = 0$. Meanwhile, their self-collision effects make the distribution function form an isotropic Maxwellian distribution. During this process, the kinetic energy of the counterstreaming plasma flows is converted into the ion internal energy, resulting in an increase in the ion temperature. In Fig. 2(b) and Fig. 2(e), a slight deviation of the distribution functions from the equilibrium state can be observed. This is because the collision frequency increases as the relative velocity decreases, so the closer ions between two colliding plasma flows are decelerated faster in the phase space. Nevertheless, isotropic Maxwellian distributions are finally achieved at a later stage as shown in Figs. 2(c) and 2(f) since the densities of plasma flows are high enough.

In practical physical problems, especially in fusion physics, the plasma may contain multiple ion species. Therefore, it is crucial to calculate the collision processes between different ion species. Figure 3 illustrates the collision between counterstreaming light and heavy ion flows, using deuterium and carbon ions respectively. Similar to Fig.

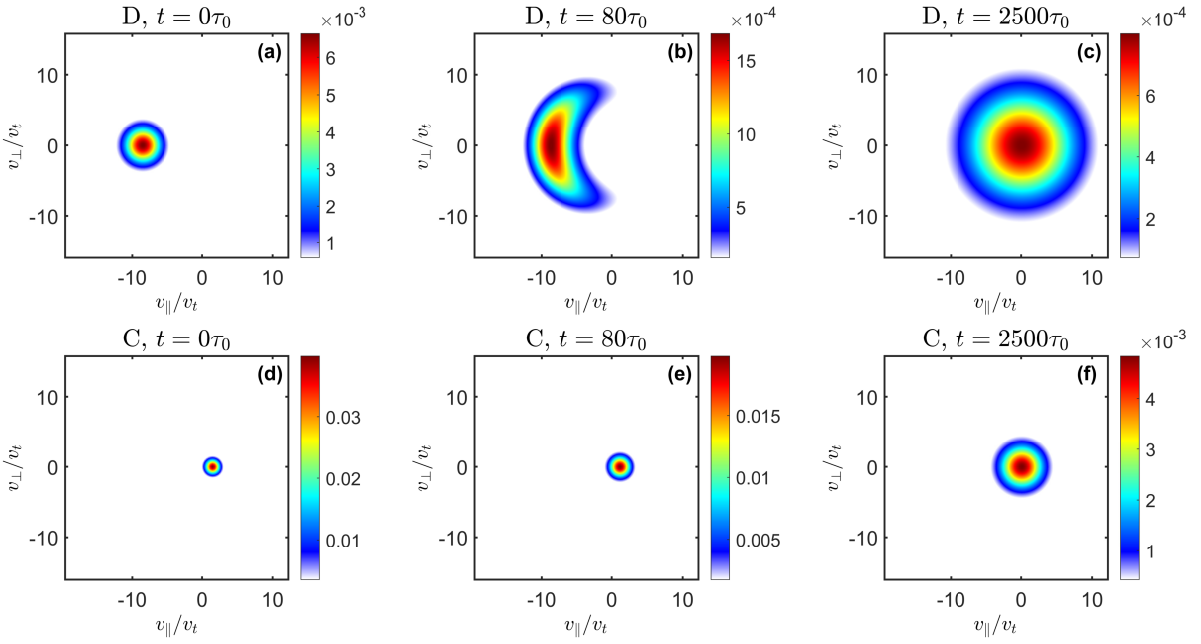

Fig. 3. Evolution of the ion distribution functions at various times. The top row is for deuterium, while the bottom row is for carbon. And the center of mass coordinate is adopted.

2, both ion species have the same initial number density and temperature as shown in Figs. 3(a) and 3(d). And the relative drift velocity between the two distribution functions is ten times the thermal velocity of the carbon ions v_t. For the light deuterium ions, their self-collision term is much smaller than the deuterium-carbon collision term. Therefore, the distribution function of the deuterium ions will be significantly distorted by the deuterium-carbon collisions and become far away from the Maxwellian distribution in the merging process. Moreover, the diffusion term is stronger than the friction term in the deuterium-carbon collision operator. As a result, the deuterium ions tend to orbit around the carbon ions with a distinct angular deflection as shown in Fig. 3(b). Finally, the distribution functions of both ion species will recover to the Maxwellian functions, at which point the drift velocities of two species of ions reduce to zero, and both ion species reach their thermal equilibrium at time $t = 2500t_0$ as shown in Figs. 3(c) and 3(f), respectively. This example shows that this numerical method can describe the collision processes between the ion species with different masses, even if their ion distribution functions deviate significantly from the equilibrium state and the relative drift velocity is much larger than their thermal velocities.

To further verify the numerical scheme for the ion-ion collision operators, we compare the FPL simulation with the multifluid model, which employs separate fluid equations for each ion species. In the multifluid model, the collisional interactions are simplified as the momentum and energy exchanges between different ion species [74, 75, 76], which can be written as

$$\begin{aligned} \mathbf{R}_{\alpha\beta} &= -m_\alpha n_\alpha \nu_{\alpha\beta} \left(\mathbf{u}_\alpha - \mathbf{u}_\beta\right), \\ Q_{\alpha\beta} &= n_\alpha m_{\alpha\beta} \nu_{\alpha\beta} \left(\mathbf{u}_\alpha - \mathbf{u}_\beta\right)^2 - n_\alpha \mu_{\alpha\beta} \left(T_\alpha - T_\beta\right). \end{aligned} \tag{33}$$

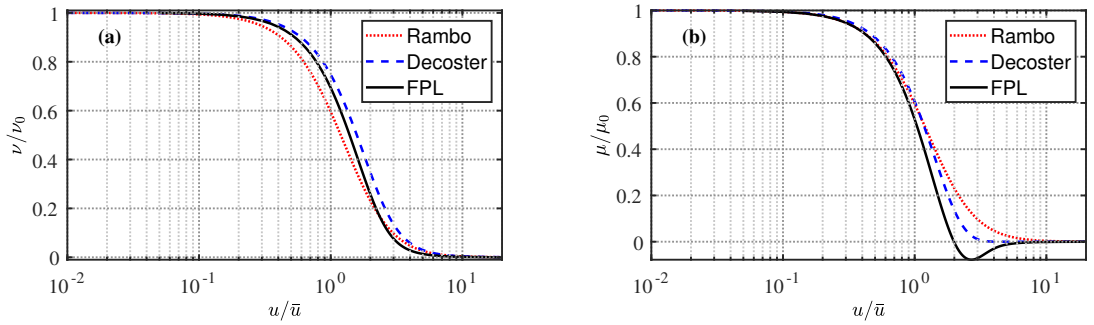

Fig. 4. The collision rate for different drift velocities, comparing the simulation (solid line) and Eqs. (34) (red dotted line) and Eqs. (35) (blue dashed line).

where $m_{\alpha\beta} = m_\alpha m_\beta/(m_\alpha + m_\beta)$ is the reduced mass, and the coefficients $\nu_{\alpha\beta}$ and $\mu_{\alpha\beta}$ is given by Rambo:

$$\nu_{\alpha\beta} = \nu^0_{\alpha\beta}\left\{1 + \left(\frac{2}{9\pi}\right)^{1/3}\bar{u}^2\right\}^{-3/2}, \quad \mu_{\alpha\beta} = \mu^0_{\alpha\beta}\left\{1 + \left(\frac{2}{9\pi}\right)^{1/3}\bar{u}^2\right\}^{-3/2}, \tag{34}$$

$$\nu^0_{\alpha\beta} = \frac{4\sqrt{2\pi}Z^2_\alpha Z^2_\beta e^4 L n_{\alpha\beta} n_\beta}{3m_{\alpha\beta}m_\alpha\left(T_\alpha/m_\alpha + T_\beta\big/m_\beta\right)^{3/2}}, \quad \mu^0_{\alpha\beta} = \frac{3m_{\alpha\beta}\nu^0_{\alpha\beta}}{m_\beta},$$

$$\bar{u} = \frac{\left|\mathbf{u}_\alpha - \mathbf{u}_\beta\right|}{\left(T_\alpha/m_\alpha + T_\beta\big/m_\beta\right)^{1/2}},$$

and Decoster [77]:

$$\nu_{\alpha\beta} = \nu^0_{\alpha\beta}\frac{3}{z^3}\int_0^z s^2 e^{-s^2/2} ds, \quad \mu_{\alpha\beta} = \mu^0_{\alpha\beta} e^{-z^2/2}. \tag{35}$$

Here the coefficients can be considered as a simple modified collision rate. When the relative drift velocity is small compared to the thermal velocity, this rate reduces to the expression derived by Braginskii for a drifting Maxwellian. When the particles drift very fast, this rate reduces to the slowing down rate for the cold plasma flows. As shown in Fig. 4 (a), the rate $\nu_{\alpha\beta}$ predicted by Eqs. (34) and Eqs. (35) coincides well with that obtained from our FPL simulations in the range of $u/\bar{u}$ from 0 to 20.

Further, the coefficient $\mu_{\alpha\beta}$ in Eqs. (33) describes the energy exchange between the ion species α and β due to their different temperatures. Interestingly, the coefficient $\mu_{\alpha\beta}$ obtained from our FPL simulations will become negative at around $u/\bar{u} = 2$ as shown in Fig. 5(b), which indicates that the energy flows from a colder plasma to a hotter plasma in this region. This seems violate the second law of thermodynamics that heat cannot spontaneously flow from a colder to a hotter reservoir but only with the expenditure of mechanical energy. It is important to point out that here the energy flowing from the colder plasma to the hotter plasma is at the expenses of the kinetic energy of the plasma flows. Since the evolution of the particle velocity distributions is accurately treated, the FPL simulations can self-consistently describe the energy exchange between two plasma flows with different temperatures. In contrast, the multifluid model only works well at the "fast" and "slow" limits, but it fails to describe the energy exchange at around $u/\bar{u} = 2$ where the particle velocity distribution function is significantly distorted and far away from the (drifting) Maxwellian distribution.

In Fig. 5, we show that the multifluid model may also fail to describe the merging process of the two colliding plasma flows that have the same ion species but different ion densities. When the initial conditions of the two plasma flows are the same ($m_\alpha = m_\beta$, $Z_\alpha = Z_\beta$, $n_\alpha = n_\beta$, $T_\alpha = T_\beta$, $\left|\mathbf{u}_\alpha - \mathbf{u}_\beta\right| = 10v_t$), the velocity (Fig. 5(a)) and temperature (Fig. 5(c)) relaxation processes obtained from the FPL simulation are similar to the results from the multifluid model. This is because in this case the velocity distribution of each plasma flow deviates only slightly from the equilibrium state as shown in Fig. 5(e) at $t = 400t_0$. However, when the densities of these two plasma flows are significantly

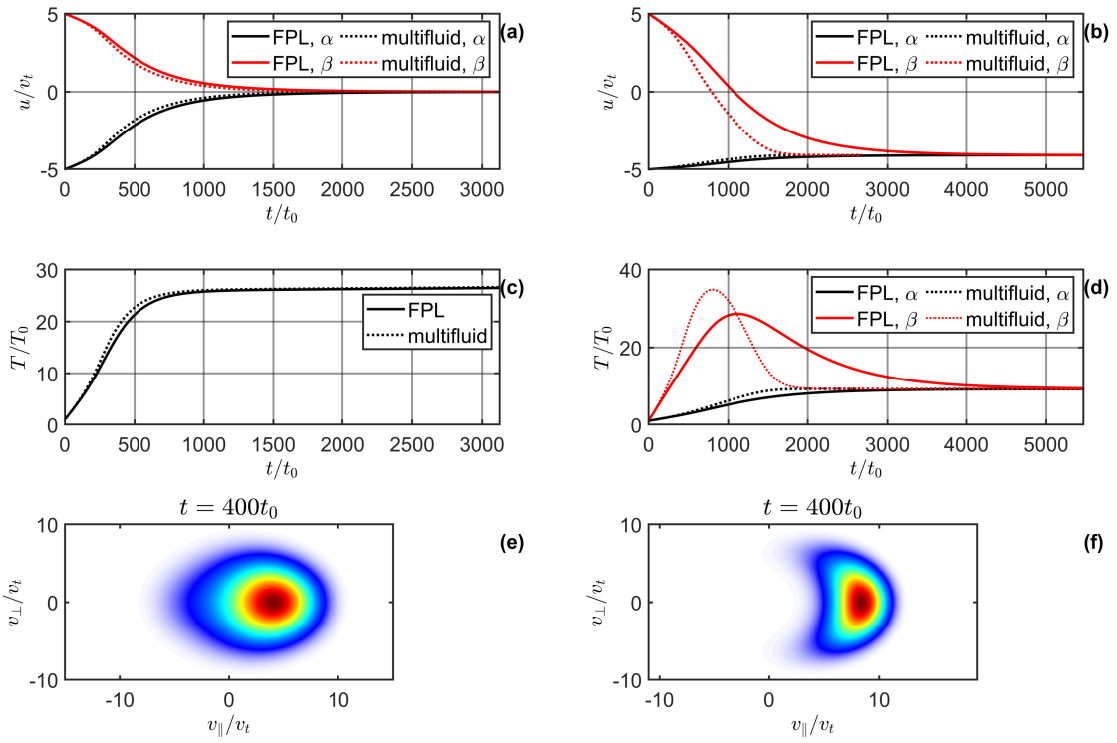

Fig. 5. Particle slowing-down processes in the homogeneous plasma. The initial conditions corresponding to (a), (c), and (e) are $m_\alpha = m_\beta$, $Z_\alpha = Z_\beta$, $n_\alpha = n_\beta$, $T_\alpha = T_\beta$, $|\mathbf{u}_\alpha - \mathbf{u}_\beta| = 10v_t$, while those corresponding to (b), (d), and (f) are $m_\alpha = m_\beta$, $Z_\alpha = Z_\beta$, $n_\alpha = 10n_\beta$, $T_\alpha = T_\beta$, $|\mathbf{u}_\alpha - \mathbf{u}_\beta| = 10v_t$. (a) and (b) show the drift velocities as functions of time, whereas (c) and (d) depict the evolution of temperature over time. (e) and (f) represent the distribution functions of β at $t = 400t_0$. In the curve chart, the black line corresponds to particle α and the red line donates particle β; the solid lines represent the FPL simulation results, while the dotted lines show the multifluid simulation results.

different, for an example $n_\alpha = 10n_\beta$, Fig. 5(b) and Fig. 5(d) show that the merging process predicted by the multifluid model will be significantly faster than that obtained from the kinetic simulation. In particular, the difference between the FPL simulation and the multifluid model is more obvious for the plasma flow with a lower density. This is because the velocity distribution of the plasma flow with a lower density will deviate more significantly from the equilibrium state. As shown in Fig. 5(f), the velocity distribution of the rare plasma flow even splits into two parts at $t = 400t_0$. The small part that is closer to the dense plasma flow in the phase space will form a Maxwellian distribution firstly, while another large part becomes significantly distorted. Even though the average flow velocity of the rare plasma flow is already small, most of the particles in the rare plasma flow are still distributed far from the dense plasma flow. Therefore, the effective collision frequency will be obviously smaller than that predicted by the multifluid model. Consequently, the multifluid model obviously overestimates the speed of the merging process of the two colliding plasma flows with significantly different densities. Similarly, the multifluid model will fail when the masses $m_{\alpha,\beta}$ or the ionization degree $Z_{\alpha,\beta}$ are significantly different. These simulation examples demonstrate the importance of considering non-equilibrium velocity distribution, and the kinetic simulation is necessary to accurately describe the merging process of the two colliding plasma flows.

3.4. Method to deal with the electron collision term

As shown in Sec. 2, the electron-electron collisions in a degenerated dense plasma can be described by the quantum FPL operator given by Eq. (11). Fortunately, the fast spectral method is also applicable to the quantum FPL operator. Following Hu et al. [53], we replace $f_e(\mathbf{v})\left[1 - \theta_e f_e(\mathbf{v})\right]$ in Eq. (11) with a new function $h(\mathbf{v})$, and a similar

convolution sum for the quantum FPL operator is given by

$$\begin{aligned}\hat{C}_{ee,\mathbf{k}} = &\sum_{\mathbf{m}=-N}^{N} \hat{f}_{\mathbf{k}-\mathbf{m},\alpha}\hat{h}_{\mathbf{m},\beta}(\mathbf{k}-\mathbf{m})^2 F(\mathbf{m}) - \sum_{\mathbf{m}=-N}^{N} \hat{h}_{\mathbf{k}-\mathbf{m},\alpha}\hat{f}_{\mathbf{m},\beta} B_L(\mathbf{m},\mathbf{m}) \\ &- \sum_{\mathbf{m}=-N}^{N}\sum_{p,q=1}^{d} \hat{f}_{\mathbf{k}-\mathbf{m},\alpha}\hat{h}_{\mathbf{m},\beta} I_{pq}(\mathbf{m})\left(k_p - m_p\right)\left(k_q - m_q\right) \\ &+ \sum_{\mathbf{m}=-N}^{N}\sum_{p=1}^{d} \hat{h}_{\mathbf{k}-\mathbf{m},\alpha}\hat{f}_{\mathbf{m},\beta} G_p(\mathbf{m},\mathbf{m})\left(k_p - m_p\right) \\ &+ \sum_{\mathbf{m}=-N}^{N}\sum_{p=1}^{d} \hat{f}_{\mathbf{k}-\mathbf{m},\alpha}\hat{h}_{\mathbf{m},\beta} G_p(\mathbf{m},\mathbf{m})\left(k_p - m_p\right).\end{aligned} \tag{36}$$

This summation approaches the classical one as $h(\mathbf{v})$ approaches $f_e(\mathbf{v})$. In Fig. 6, we show an example to calculate the quantum electron collision term with this model from classical to strong degeneracy region, where the distribution evolves from an initial non-equilibrium distribution. Finally, the distribution reaches the equilibrium and is consistent with the Fermi-Dirac distribution. In addition, when the degeneracy effect is strong, the gradient of the distribution function in the phase space is also steep, which means that smaller Δv and Δt are needed in the phase space.

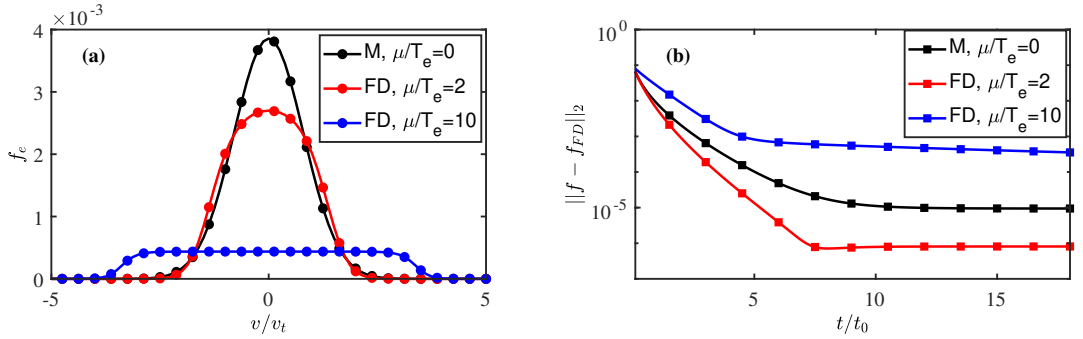

Fig. 6. (a) The velocity distribution functions obtained from simulation (dots) at $t = 5t_0$ with different μ/T. (b) The time evolution for different μ/T with the non-equilibrium initial distribution.

3.5. Collision between ions and electrons

The ion-electron collisions and electron-ion collisions are described by the simplified operators Eq. (15) and Eq. (16), respectively. Meanwhile, they must conserve energy and momentum:

$$\begin{aligned}&\mathbf{R}_{e\alpha} + \mathbf{R}_{\alpha e} = 0, \\ &Q_{\alpha e} + Q_{e\alpha} = -\mathbf{R}_{\alpha e}\cdot(\mathbf{u}_\alpha - \mathbf{u}_e),\end{aligned} \tag{37}$$

where the friction and heat can be calculated as follows

$$\begin{aligned}\mathbf{R}_{e\alpha} &= -\frac{m_e n_e}{\tau_{ei}}(\mathbf{u}_e - \mathbf{u}_\alpha), \\ Q_{e\alpha} &= \frac{m_e n_e}{\tau_{ei}}(\mathbf{u}_e - \mathbf{u}_\alpha)^2 - \frac{3m_e}{m_\alpha}\frac{n_e}{\tau_{ei}}(T_e - T_\alpha).\end{aligned} \tag{38}$$

Then, the local Maxwellian distribution $\bar{f}$ in the Krook model Eq.(16) can be updated by using the momentum and temperature calculated above. In addition, it is necessary to know the fugacity $z = \exp(-\mu/T)$ and temperature T to calculate the relaxation time τ_{ei} in Eq. (15). For quantum gas, these two variables are connected with the density n_e and internal energy e_e as

$$n_e = \frac{(2\pi T_e)^{3/2}}{\theta_e} F_{3/2}(z), \quad e_e = \frac{3}{2} T_e \frac{F_{5/2}(z)}{F_{3/2}(z)}, \tag{39}$$

where $F_i(z)$ is the Fermi-Dirac function, and z can be computed by cubic spline interpolation.

3.6. All collisions included in a homogeneous plasma

The collision equations for the ions and the electrons are discreted in time, in which the ion-ion and electron-electron collision terms are treated explicitly, while the penalization function, ion-electron, and electron-ion collision terms are treated implicitly. Thus the discreted collision equations look like:

$$\begin{aligned}\frac{f_\alpha^{n+1}-f_\alpha^n}{\Delta t} &= \sum_\beta C_{\alpha\beta}^n\left(f_\alpha^n\right)-\zeta^n P^n\left(f_\alpha^n\right)+\zeta^n P^{n+1}\left(f_\alpha^{n+1}\right)+C_{ie}^{n+1}\left(f_\alpha^{n+1}\right),\\ \frac{f_e^n-f_e^n}{\Delta t} &= C_{ee}^n\left(f_e^n\right)-\zeta^n P^n\left(f_e^n\right)+\zeta^{n+1} P^{n+1}\left(f_e^{n+1}\right)+C_{ei}^{n+1}\left(f_e^{n+1}\right).\end{aligned} \tag{40}$$

The explicit FPL operators can be calculated by using Eq. (27) and Eq. (36) as

$$\begin{aligned}C_{\alpha\beta}^n\left(f_\alpha^n,f_\beta^n\right) &= \mathcal{F}^{-1}\left[\hat{C}_{\alpha\beta}\left(f_\alpha^n,f_\beta^n\right)\right],\\ C_{ee}^n\left(f_e^n\right) &= \mathcal{F}^{-1}\left[\hat{C}_{ee}\left(f_e^n\right)\right],\end{aligned} \tag{41}$$

where $\mathcal{F}$ is the Fourier transform. In the ion-electron collision term, we treat the density, temperature, and drift velocity explicitly with:

$$C_{ie}^{n+1}\left(f_\alpha^{n+1}\right)=\frac{n_e^n\mu_0}{A_\alpha n_\alpha^n}\frac{1}{\tau_{ei}^n}\frac{\partial}{\partial v_\beta}\left(\left(v_\beta-u_{e,\beta}^n\right)f_\alpha^{n+1}+\frac{T_e^n}{A_\alpha}\frac{\partial f_\alpha^{n+1}}{\partial v_\beta}\right), \tag{42}$$

and the derivatives of the distribution function are discretized using a finite-difference scheme as

$$\begin{aligned}\left.\frac{\partial f}{\partial v}\right|_i &= \frac{f\left(v_{i+1}\right)-f\left(v_{i-1}\right)}{2\Delta v},\\ \left.\frac{\partial^2 f}{\partial v^2}\right|_i &= \frac{f\left(v_{i+1}\right)+f\left(v_{i-1}\right)-2f\left(v_i\right)}{\Delta v^2}.\end{aligned} \tag{43}$$

For the electron-ion collision term, we treat the equilibrium distribution function $\bar{f}$ explicitly in which the energy and momentum are updated according to the conservation Eqs. (38)

$$C_{ei}^{n+1}\left(f_e^{n+1}\right)=-\frac{1}{\tau_{ei}^n}\left(f_e^{n+1}-\bar{f}^n\right). \tag{44}$$

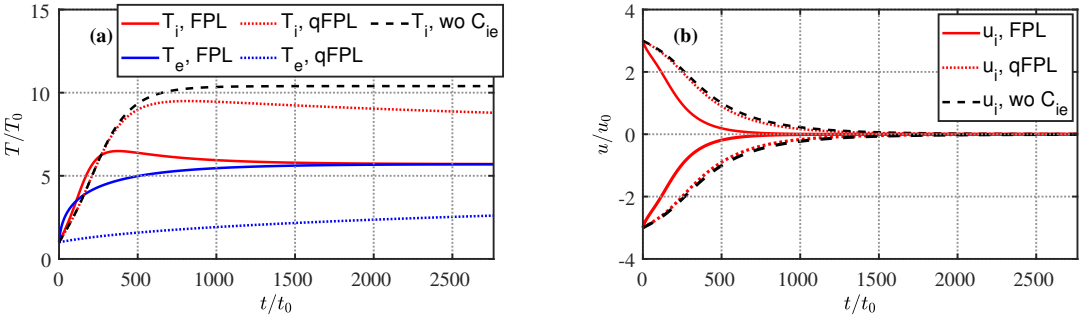

Fig. 7. Evolution of counterstreaming plasma described by the temperature and drift velocity. (a) Temperature, where the solid red lines represent ions and the solid blue lines show the electron temperature with the classical collision operator; The dotted line shows the temperatures for ions (red) and electrons (blue) when the electron degeneracy effect is included. (b) The drift velocity, where the black dashed lines ignore ion-electron collisions.

Combining the above equaitons, we can simultaneously consider the collision effects between all particle species in a homogeneous plasma. In Fig. 7, we simulate the collision processes between the counterstreaming plasma

flows with all collision terms included. Here, the two plasma flows have the same initial density and electron and ion temperatures, and the relative drift speed between them is approximately 6 times the ion thermal velocity v_t. Figures 7(a) and 7(b) present the time evolution of temperatures and drift velocity, respectively. It is found that the isotropization of the ions dominates at the first stage, in which the kinetic energy of the ions is converted into the ion thermal energy. However, a part of the ion kinetic energy will also be transferred to the electrons if the electron-ion collisions are considering, causing the final steady-state ion temperature to decrease as compared to the case without the electron-ion collisions. Meanwhile, the electron temperature will rapidly increase due to the collisions with the ions. At the second stage, the ion thermal energy will be gradually converted into the electron thermal energy due to the thermalization until the ion and electron temperatures become equal. Furthermore, Fig. 7(b) shows that the electrons have a significant deceleration effect upon the ions. However, this effect has almost disappeared when the degeneracy effect is included. In the quantum degeneracy case, we take the initial parameters of $A = 2$, $Z = 1$, $n = 4 \times 10^{25}$ cm^{-3}, and $T = 50$eV. With these parameters, the degeneracy parameter T/E_F is approximately 0.1, and the effective collision frequency calculated by Eq. (13) is only 0.015 times of its classical limit. Therefore, it can be seen that the degeneracy effects have an evident influence on the merging process of two colliding supersonic dense plasma flows.

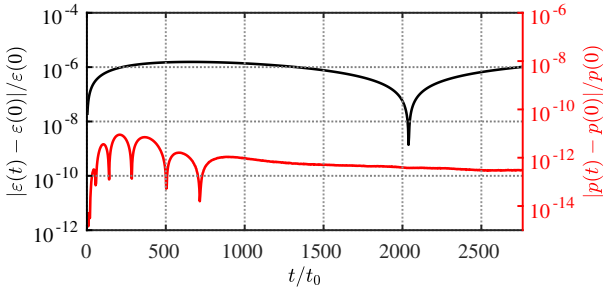

Fig. 8. The evolution of total energy deviation (black line) and momentum deviation (red line) over time for the case corresponding to the classical limit presented in Fig. 7.

As mentioned earlier, the fast spectral method does not strictly guarantee the conservation of energy and momentum. In Fig. 8, we illustrate the variation of energy and momentum error over time from the simulation in Fig. 7. The results indicate that although the conservation of total energy and momentum is not perfect, it is still acceptable. To completely eliminate all errors, we recommend a remediation method proposed in Ref. [39]. This approach evaluates the errors in energy and momentum generated by collision terms at each timestep, and feed this discrepancy back to the electrons to guarantee the conservation of energy and momentum.

4. Numerical examples

In this section, we present numerical test results with 1D or 2D coordinate space. In the simulations, periodic boundary conditions are implemented along the x- and y-directions in the coordinate space. Zero boundary conditions are applied in the velocity space, i.e. $f(|v| > v_{bound}) = 0$, where v_{bound} is a large enough velocity. Further, the simulation code is parallelized, where the simulation domain is divided into several sub-domains in the coordinated space, while the velocity space is not decomposed. We implement a Message Passing Interface (MPI) to communicate the values of the distributions at the adjacent space between sub-domains in individual computational nodes. And Fig. 9 (a) shows an example of the MPI domain division. The OpenMP is used to realize the multi-thread parallelization between CPU cores at each node. Since the computational cost is mainly spent on the collision operators, we can solve the VFPL equation with the collision terms only in a part of the coordinate space. At the spatial grids where the collision time is very long, the Vlasov equation that is greatly simplified for collisionless plasmas is solved instead of the VFPL equation (Fig. 9(b)). In the following simulations, the collision operators are not considered in the region with $n_i/v_t^3 < 10^{-6} n_0/v_0^3$.

4.1. One-dimensional simulation

In the following, we simulate the collision of two high-density hydrogen plasma flows with finite sizes in the 1D coordinate space. The hydrogen plasma flows have the same initial temperature $T = 300$eV, the same drift speed

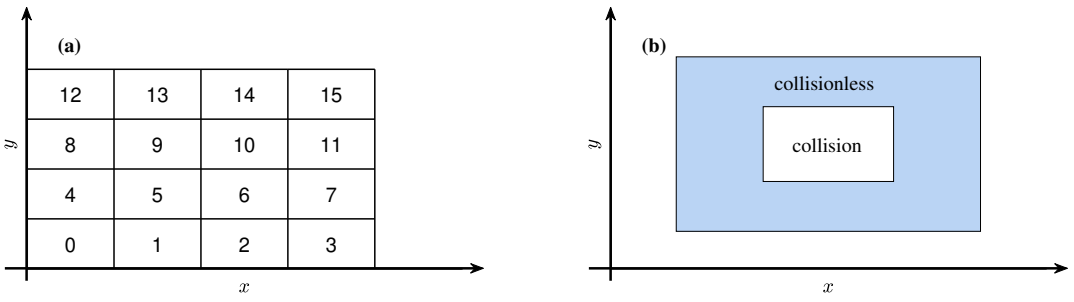

Fig. 9. (a) Arrangement of MPI process. (b) Schematic diagram of 'collision domain' and 'collisionless' domain.

500km/s, and the similar Gaussian density profiles $n_i(x) = n_0 \exp[-(x - x_{L0,R0})^2/2\sigma^2]$ with σ=5μm, where x_{L0} and x_{R0} are the initial center coordinates of the left and right plasma flows, respectively. The plasma drift, collision, and expansion during the merging of these two plasma flows are compared with different initial flow peak densities n_0. For the convenience of analysis, the ions in the left and right plasma flows are described by two independent velocity distribution functions in the simulations. Figure 10 illustrates the spatiotemporal evolution of the ion density of the left plasma flow, while the ion density of the right plasma flow is symmetrical.

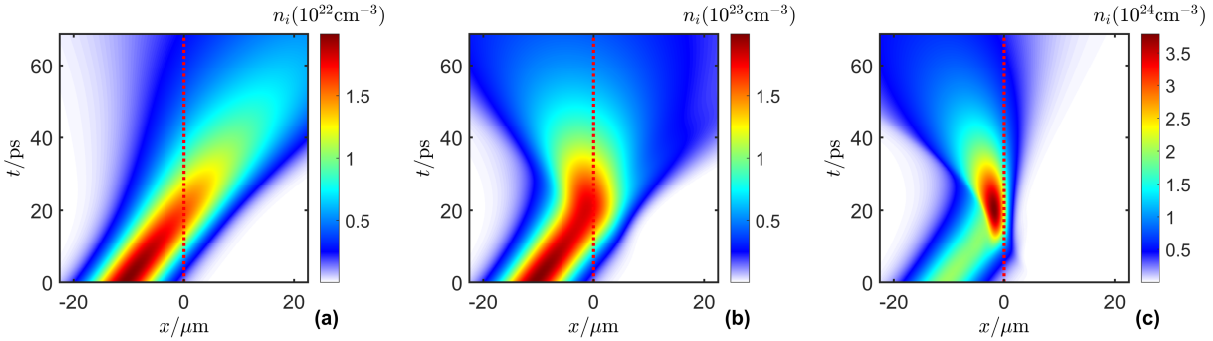

Fig. 10. The temporal evolution of one-dimensional spatial distributions of ion density. Figures (a), (b), and (c) correspond to the initial densities of $2 \times 10^{22} cm^{-3}$, $2 \times 10^{23} cm^{-3}$, and $2 \times 10^{24} cm^{-3}$, respectively.

It can be observed that when the density is relatively low as $n_0 = 2 \times 10^{22}\mathrm{cm}^{-3}$, the left plasma flow will directly pass through the center position $x = 0$ with a slight thermal expansion, i.e. it is almost unaffected by the right plasma flow, as shown in Fig. 10(a). When the initial density increases to $n_0 = 2 \times 10^{23}$ cm^{-3}, the left plasma flow will be stopped at around $x = 0$ with an obvious thermal expansion as shown in Fig. 10(b)). At such a high density, the mean-free path of the ions is on the order of 10μm, which is as short as the size of the plasma flows. Therefore, the plasma flows are barely able to pass through each other. Moreover, the plasma temperature greatly increases because the kinetic energy of the plasma flow is converted into its thermal energy, leading to the enhanced plasma thermal expansion. Increasing the initial density further by an order of magnitude to $n_0 = 2 \times 10^{24}\mathrm{cm}^{-3}$, the strong collisions will result in an ultra short mean-free path for the ions. Consequently, Fig. 10(c) shows that the left plasma flow will be stopped even before it reaches the center, resulting in a density accumulation in a relatively broad region. Such a stagnation stage can sustain for about 20ps, followed by the thermal expansion towards the reverse direction.

The energy exchanges between the ion kinetic and thermal energies as well as between the ions and the electrons are illuminiated in Fig. 11. Since our simulation code can conserve the energy quite well, the total energy in the whole simulation box is nearly constant during the collision of two plasma flows in each simulation case. Figure 11(a) shows that both the ion kinetic energy and temperature change little, indicating that the plasma flows can pass through each other nearly without let or hindrance at the relatively low density $n_0 = 2 \times 10^{22}\mathrm{cm}^{-3}$. At the higher density $n_0 = 2 \times 10^{23}\mathrm{cm}^{-3}$, however, the ion kinetic energy decreases significantly as shown in Fig. 11(b). At

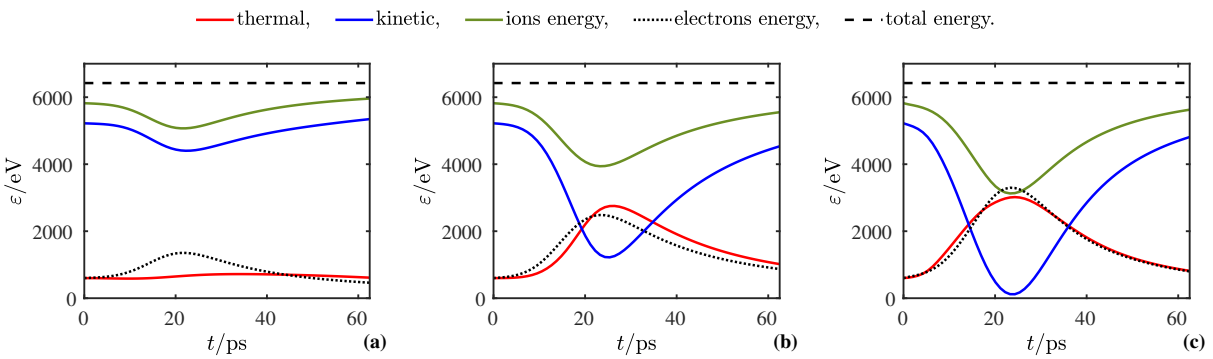

Fig. 11. The temporal evolution of the spatially averaged energy, where the spatial average value of the quantity $\bar{Q}(t)$ is defined as $\int n(x,t)\,Q(x,t)\,dx \Big/ \int n(x,t)\,dx$. Each figure corresponds to the respective density in Fig.10. The black dashed line represents the total energy, the green solid line represents the ion energy, and the black dotted line represents the electron energy. The blue line represents the ion kinetic energy, while the red line represents the ion thermal energy.

$t = 25$ps, the thermal energy even exceeds the kinetic energy. Later, the ion kinetic energy will reversely increase due to plasma expansion. At the highest density $n_0 = 2\times10^{24}\mathrm{cm}^{-3}$, Fig. 11(c) shows that nearly all the ion kinetic energy can be dissipated into the thermal energy due to the ultra-strong collisions. Furthermore, a large proportion of the ion kinetic energy is transferred to the electrons rather than the ion thermal energy since the electron-ion collisions become very efficient in such a high density plasma. The above tests verify that our VFPL code can simulate the colliding supersonic dense plasma flows well, and the processes of energy conversion and deposition are described properly.

4.2. Two-dimensional simulation

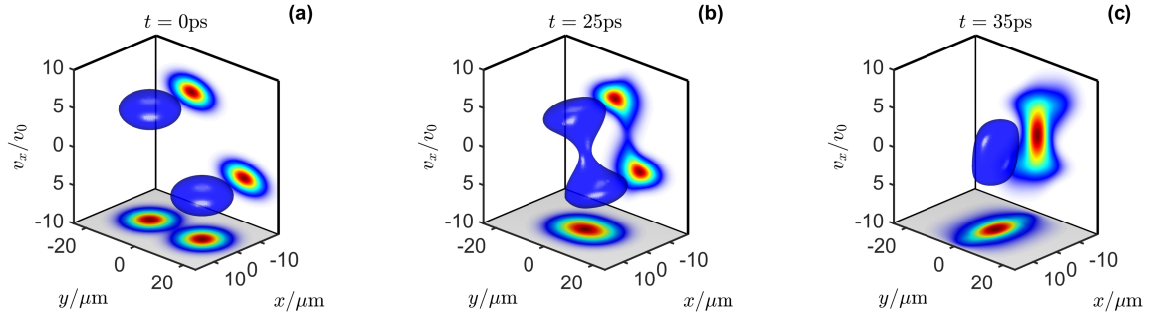

Fig. 12. A two-dimensional simulation of counterstreaming plasma blocks with initial $n_i = 10^{23}\mathbf{cm}^{-3}$, $T = 300\mathbf{eV}$ and $u_x = 500\mathbf{km/s}$, where (a), (b), and (c) are the different snapshot of distribution function $\int_{-\infty}^{\infty} f(\mathbf{x},\mathbf{v})\,dv_y$ in the phase space (blue surface) and their projections in x-y and x-v_x plane at $t = 0\mathbf{ps}$, $t = 25\mathbf{ps}$, and $t = 35\mathbf{ps}$, respectively.

Finally, we utilize the VFPL code with two spatial coordinates to simulate the collision between two colliding plasma blocks. In Fig. 12, we show the ion velocity distribution integrated over the v_y at three typical moments to illustrate the merging process of the colliding plasma blocks in the x-y-v_x phase space. In contrast to 1D simulations, the ions suffer a strong expansion in the y-direction in the 2D simulation. Therefore, the ion density distribution has the shape of an ellipse in the x-y space at $t = 35$ps after the merging. More importantly, the maximum ion density is much smaller than twice the initial ion density as shown in Fig. 13(a). Further, Fig. 13(b) displays the energy conversion as well as the conservation of the total energy. Due to the enormous computational cost, we do not employ two ion distribution functions in the 2D2V simulation. As a result, it is difficult to distinguish between the ion kinetic energy and the ion thermal energy. Instead, the effective ion temperatures that perpendicular T_y and parallel T_x to the initial drift velocity are employed. Figure 13(b) shows that the longitudinal ion temperature T_x decreases while the

transverse ion temperature T_y and electron energy increase with time. This indicates the conversion of the ion kinetic energy into the ion thermal energy and the electron thermal energy. As expected, Fig. 13(b) also shows that the energy conservation is maintained well in this 2D simulation. This test verifies that our 2D2V VFPL code has the ability to simulate the colliding supersonic dense plasma flows on the spatio-temporal scale of tens of microns and hundreds of picoseconds.

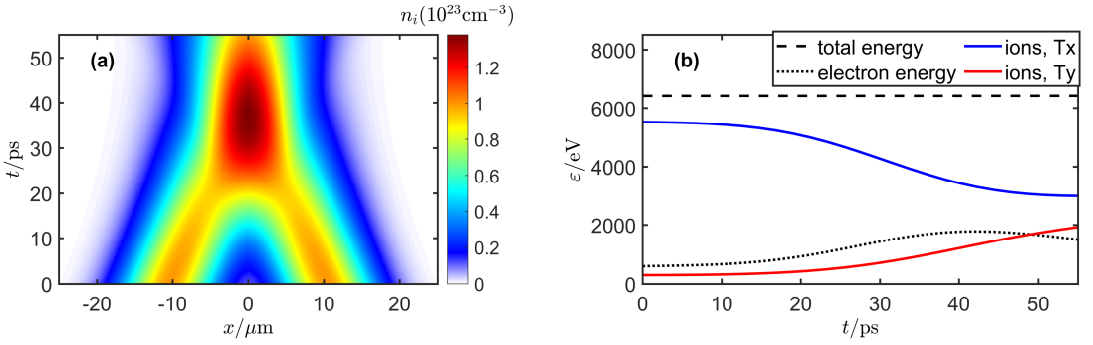

Fig. 13. The temporal evolution of (a) spatial distributions of ion density at y=0, and (b) the spatially averaged energy, corresponding to simulation Fig. 12. The black dashed line represents the total energy, and the black solid line represents the electron energy. The blue line and the red line represents $T_x = \int_{-\infty}^{\infty} f(\mathbf{x},\mathbf{v})\, v_x^2 d\mathbf{v}$ and $T_y = \int_{-\infty}^{\infty} f(\mathbf{x},\mathbf{v})\, v_y^2 d\mathbf{v}$ for ions, respectively.

5. Conclusions

In conclusion, we have developed 1D2V and 2D2V Vlasov-Fokker-Planck-Landau codes to model the kinetic dynamics of two colliding supersonic dense plasma flows/blocks. Both the ions and electrons are treated kinetically in the codes, where the Fokker-Planck-Landau collision operators are applied both for the electrons and ions. A simplified ion-electron collision operator is applied, which can capture the exchange of momentum and energy between the electrons and ions. The fast spectral method and the asymptotic-preserving scheme are adopted to solve the Fokker-Planck-Landau equation, which balance the efficiency and the accuracy well. Consequently, the conservation of the mass, momentum, and energy is well satisfied. The fast spectral method can also work well with the electron quantum degeneracy effect included. The codes allow us to simulate the ion and electron collisions with a reasonable time step at a relatively high computing speed and time step, which may be used to simulate various problems involving high-speed dense plasma flows/blocks. Moreover, our code has the capability to deal with plasma flows drifting at velocities twenty times greater than the thermal velocity. However, when the flow velocity is increased further, the simulations will be limited by the large amount of computational cost. This is because a greater number of meshes in velocity space are required when the plasma temperature is increased significantly during the interaction. To overcome this issue, one may adopt the moving-grid strategy, which allows for the calculation of plasmas with higher Mach numbers. In this approach, one may adapt the mesh sizes in velocity space with time to maintain a reasonable computing efficiency. Interested readers may refer to Refs. [30, 78] on the semi-Lagrangian method and Vlasov-Fokker-Planck equation on a moving grid.

Acknowledgments

This work is supported by the Strategic Priority Research Program of Chinese Academy of Sciences (Grant No. XDA25050100 and XDA25010100) and the Science Challenge Project (No. TZ2018005).

References

[1] A. Marcowith, A. Bret, A. Bykov, M. E. Dieckman, L. O. Drury, B. Lembege, M. Lemoine, G. Morlino, G. Murphy, G. Pelletier, et al., The microphysics of collisionless shock waves, Reports on Progress in Physics 79 (2016) 046901.

[2] H.-S. Park, D. Ryutov, J. Ross, N. Kugland, S. Glenzer, C. Plechaty, S. Pollaine, B. Remington, A. Spitkovsky, L. Gargate, et al., Studying astrophysical collisionless shocks with counterstreaming plasmas from high power lasers, High Energy Density Physics 8 (2012) 38–45.

[3] J. Ross, S. Glenzer, P. Amendt, R. Berger, L. Divol, N. Kugland, O. Landen, C. Plechaty, B. Remington, D. Ryutov, et al., Characterizing counter-streaming interpenetrating plasmas relevant to astrophysical collisionless shocks, Physics of Plasmas 19 (2012) 056501.

[4] A. Spitkovsky, Simulations of relativistic collisionless shocks: shock structure and particle acceleration, in: AIP Conference Proceedings, volume 801, American Institute of Physics, 2005, pp. 345–350.

[5] D. Montgomery, G. Joyce, Shock-like solutions of the electrostatic vlasov equation, Journal of Plasma Physics 3 (1969) 1–11.

[6] J. M. Stone, M. L. Norman, Zeus-2d: a radiation magnetohydrodynamics code for astrophysical flows in two space dimensions. i-the hydrodynamic algorithms and tests., Astrophysical Journal Supplement Series (ISSN 0067-0049), vol. 80, no. 2, June 1992, p. 753-790. Research supported by University of Illinois. 80 (1992) 753–790.

[7] Y. Kuramitsu, Y. Sakawa, T. Morita, C. Gregory, J. Waugh, S. Dono, H. Aoki, H. Tanji, M. Koenig, N. Woolsey, et al., Time evolution of collisionless shock in counterstreaming laser-produced plasmas, Physical review letters 106 (2011) 175002.

[8] C. Li, D. Ryutov, S. Hu, M. Rosenberg, A. Zylstra, F. Séguin, J. Frenje, D. Casey, M. G. Johnson, M.-E. Manuel, et al., Structure and dynamics of colliding plasma jets, Physical Review Letters 111 (2013) 235003.

[9] G. Chabrier, F. Douchin, A. Potekhin, Dense astrophysical plasmas, Journal of Physics: Condensed Matter 14 (2002) 9133.

[10] B. A. Remington, R. P. Drake, D. D. Ryutov, Experimental astrophysics with high power lasers and z pinches, Reviews of Modern Physics 78 (2006) 755.

[11] R. Bosch, R. Berger, B. Failor, N. Delamater, G. Charatis, R. Kauffman, Collision and interpenetration of plasmas created by laser-illuminated disks, Physics of Fluids B: Plasma Physics 4 (1992) 979–988.

[12] M. Casanova, O. Larroche, J.-P. Matte, Kinetic simulation of a collisional shock wave in a plasma, Physical review letters 67 (1991) 2143.

[13] D. Ryutov, N. Kugland, H.-S. Park, C. Plechaty, B. Remington, J. Ross, Intra-jet shocks in two counter-streaming, weakly collisional plasma jets, Physics of Plasmas 19 (2012) 074501.

[14] M. N. Rosenbluth, W. M. MacDonald, D. L. Judd, Fokker-planck equation for an inverse-square force, Physical Review 107 (1957) 1.

[15] L. D. Landau, THE KINETIC EQUATION IN THE CASE OF COULOMB INTERACTION., Technical Report, General Dynamics/Astronautics San Diego Calif, 1958.

[16] A. Bell, A. Robinson, M. Sherlock, R. Kingham, W. Rozmus, Fast electron transport in laser-produced plasmas and the kalos code for solution of the vlasov–fokker–planck equation, Plasma Physics and controlled fusion 48 (2006) R37.

[17] E. Epperlein, G. Rickard, A. Bell, A code for the solution of the vlasov-fokker-planck equation in 1-d or 2-d, Computer physics communications 52 (1988) 7–13.

[18] R. Kingham, A. Bell, An implicit vlasov–fokker–planck code to model non-local electron transport in 2-d with magnetic fields, Journal of Computational Physics 194 (2004) 1–34.

[19] A. Thomas, M. Tzoufras, A. Robinson, R. J. Kingham, C. Ridgers, M. Sherlock, A. Bell, A review of vlasov–fokker–planck numerical modeling of inertial confinement fusion plasma, Journal of Computational Physics 231 (2012) 1051–1079.

[20] M. Tzoufras, A. Bell, P. Norreys, F. Tsung, A vlasov–fokker–planck code for high energy density physics, Journal of Computational Physics 230 (2011) 6475–6494.

[21] S. Weng, Z.-M. Sheng, M. He, J. Zhang, P. Norreys, M. Sherlock, A. Robinson, Plasma currents and electron distribution functions under a dc electric field of arbitrary strength, Physical review letters 100 (2008) 185001.

[22] H. Zhao, Z. Sheng, S. Weng, Nonlocal thermal transport in magnetized plasma along different directions, Matter and Radiation at Extremes 7 (2022) 045901.

[23] S.-M. Weng, Z.-M. Sheng, J. Zhang, Inverse bremsstrahlung absorption with nonlinear effects of high laser intensity and non-maxwellian distribution, Physical Review E 80 (2009) 056406.

[24] S.-M. Weng, Z.-M. Sheng, H. Xu, J. Zhang, Vlasov-fokker-planck simulations for high-power laser-plasma interactions, Communications in Computational Physics 11 (2012) 1236–1260.

[25] O. Larroche, Kinetic simulation of a plasma collision experiment, Physics of Fluids B: Plasma Physics 5 (1993) 2816–2840.

[26] F. Vidal, J. Matte, M. Casanova, O. Larroche, Ion kinetic simulations of the formation and propagation of a planar collisional shock wave in a plasma, Physics of Fluids B: Plasma Physics 5 (1993) 3182–3190.

[27] F. Vidal, J. Matte, M. Casanova, O. Larroche, Spherical ion kinetic simulations of dt implosions, Physical Review E 52 (1995) 4568.

[28] O. Larroche, Kinetic simulations of fuel ion transport in icf target implosions, The European Physical Journal D-Atomic, Molecular, Optical and Plasma Physics 27 (2003) 131–146.

[29] O. Larroche, Ion fokker-planck simulation of d-3he gas target implosions, Physics of Plasmas 19 (2012) 122706.

[30] W. T. Taitano, L. Chacon, A. N. Simakov, S. E. Anderson, A conservative phase-space moving-grid strategy for a 1d-2v vlasov–fokker–planck solver, Computer Physics Communications 258 (2021) 107547.

[31] W. T. Taitano, L. Chacon, A. N. Simakov, An adaptive, implicit, conservative, 1d-2v multi-species vlasov–fokker–planck multi-scale solver in planar geometry, Journal of Computational Physics 365 (2018) 173–205.

[32] F. Filbet, L. Pareschi, A numerical method for the accurate solution of the fokker–planck–landau equation in the nonhomogeneous case, Journal of Computational Physics 179 (2002) 1–26.

[33] R. Hager, E. Yoon, S. Ku, E. F. D'Azevedo, P. H. Worley, C.-S. Chang, A fully non-linear multi-species fokker–planck–landau collision operator for simulation of fusion plasma, Journal of Computational Physics 315 (2016) 644–660.

[34] M. Murakami, H. Nagatomo, T. Johzaki, T. Sakaiya, A. Velikovich, M. Karasik, S. Gus' Kov, N. Zmitrenko, Impact ignition as a track to laser fusion, Nuclear Fusion 54 (2014) 054007.

[35] P. Velarde, F. Ogando, S. Eliezer, J. Martinez-Val, J. Perlado, M. Murakami, Comparison between jet collision and shell impact concepts for fast ignition, Laser and Particle Beams 23 (2005) 43–46.

[36] H. Nagatomo, T. Johzaki, T. Nakamura, H. Sakagami, A. Sunahara, K. Mima, Simulation and design study of cryogenic cone shell target for fast ignition realization experiment project, Physics of plasmas 14 (2007) 056303.

[37] H. Azechi, T. Sakaiya, T. Watari, M. Karasik, H. Saito, K. Ohtani, K. Takeda, H. Hosoda, H. Shiraga, M. Nakai, et al., Experimental evidence of impact ignition: 100-fold increase of neutron yield by impactor collision, Physical review letters 102 (2009) 235002.

[38] J. Zhang, W. Wang, X. Yang, D. Wu, Y. Ma, J. Jiao, Z. Zhang, F. Wu, X. Yuan, Y. Li, et al., Double-cone ignition scheme for inertial confinement fusion, Philosophical Transactions of the Royal Society A 378 (2020) 20200015.

[39] A. Bell, M. Tzoufras, Electron transport and shock ignition, Plasma Physics and Controlled Fusion 53 (2011) 045010.

[40] L. Chacón, D. Barnes, D. Knoll, G. Miley, An implicit energy-conservative 2d fokker–planck algorithm: I. difference scheme, Journal of Computational Physics 157 (2000) 618–653.

[41] A. Pataki, L. Greengard, Fast elliptic solvers in cylindrical coordinates and the coulomb collision operator, Journal of Computational Physics 230 (2011) 7840–7852.

[42] W. T. Taitano, L. Chacón, A. Simakov, K. Molvig, A mass, momentum, and energy conserving, fully implicit, scalable algorithm for the multi-dimensional, multi-species rosenbluth–fokker–planck equation, Journal of Computational Physics 297 (2015) 357–380.

[43] W. T. Taitano, L. Chacon, A. N. Simakov, An adaptive, conservative 0d-2v multispecies rosenbluth–fokker–planck solver for arbitrarily disparate mass and temperature regimes, Journal of Computational Physics 318 (2016) 391–420.

[44] L. Pareschi, G. Russo, G. Toscani, Fast spectral methods for the fokker–planck–landau collision operator, Journal of Computational Physics 165 (2000) 216–236.

[45] C. Buet, S. Cordier, P. Degond, M. Lemou, Fast algorithms for numerical, conservative, and entropy approximations of the fokker–planck–landau equation, Journal of Computational Physics 133 (1997) 310–322.

[46] M. Lemou, Multipole expansions for the fokker-planck equation, Numer. Math 78 (1998) 597–618.

[47] S. Jin, B. Yan, A class of asymptotic-preserving schemes for the fokker–planck–landau equation, Journal of Computational Physics 230 (2011) 6420–6437.

[48] S. Jin, Asymptotic-preserving schemes for multiscale physical problems, Acta Numerica 31 (2022) 415–489.

[49] J. Daligault, On the quantum landau collision operator and electron collisions in dense plasmas, Physics of Plasmas 23 (2016) 032706.

[50] D. Wu, W. Yu, S. Fritzsche, X. He, Particle-in-cell simulation method for macroscopic degenerate plasmas, Physical Review E 102 (2020) 033312.

[51] S. Brown, M. Haines, Transport in partially degenerate, magnetized plasmas. part 1. collision operators, Journal of plasma physics 58 (1997) 577–600.

[52] S. Brown, M. Haines, Transport in partially degenerate, magnetized plasmas. part 2. numerical calculation of transport coefficients, Journal of plasma physics 62 (1999) 129–144.

[53] J. Hu, S. Jin, B. Yan, A numerical scheme for the quantum fokker-planck-landau equation efficient in the fluid regime, Communications in Computational Physics 12 (2012) 1541–1561.

[54] H. Brysk, P. Campbell, P. Hammerling, Thermal conduction in laser fusion, Plasma Physics 17 (1975) 473.

[55] S. Braginskii, Transport processes in a plasma, Reviews of plasma physics 1 (1965) 205.

[56] P. L. Bhatnagar, E. P. Gross, M. Krook, A model for collision processes in gases. i. small amplitude processes in charged and neutral one-component systems, Physical review 94 (1954) 511.

[57] D. G. Colombant, W. M. Manheimer, Internal tests and improvements of the krook model for nonlocal electron energy transport in laser produced plasmas, Physics of Plasmas 17 (2010) 112706.

[58] W. Manheimer, D. Colombant, V. Goncharov, The development of a krook model for nonlocal transport in laser produced plasmas. i. basic theory, Physics of Plasmas 15 (2008) 083103.

[59] A. Mangeney, F. Califano, C. Cavazzoni, P. Travnicek, A numerical scheme for the integration of the vlasov–maxwell system of equations, Journal of Computational Physics 179 (2002) 495–538.

[60] C.-Z. Cheng, G. Knorr, The integration of the vlasov equation in configuration space, Journal of Computational Physics 22 (1976) 330–351.

[61] E. Sonnendrücker, J. Roche, P. Bertrand, A. Ghizzo, The semi-lagrangian method for the numerical resolution of the vlasov equation, Journal of computational physics 149 (1999) 201–220.

[62] T. Yabe, R. Tanaka, T. Nakamura, F. Xiao, An exactly conservative semi-lagrangian scheme (cip–csl) in one dimension, Monthly Weather Review 129 (2001) 332–344.

[63] F. Filbet, E. Sonnendrücker, P. Bertrand, Conservative numerical schemes for the vlasov equation, Journal of Computational Physics 172 (2001) 166–187.

[64] S. Tanaka, K. Yoshikawa, T. Minoshima, N. Yoshida, Multidimensional vlasov–poisson simulations with high-order monotonicity-and positivity-preserving schemes, The Astrophysical Journal 849 (2017) 76.

[65] J.-M. Qiu, C.-W. Shu, Conservative semi-lagrangian finite difference weno formulations with applications to the vlasov equation, Communications in Computational Physics 10 (2011) 979–1000.

[66] L. Chacón, D. Barnes, D. Knoll, G. Miley, An implicit energy-conservative 2d fokker–planck algorithm: Ii. jacobian-free newton–krylov solver, Journal of Computational Physics 157 (2000) 654–682.

[67] Y. A. Berezin, V. Khudick, M. Pekker, Conservative finite-difference schemes for the fokker-planck equation not violating the law of an increasing entropy, Journal of Computational Physics 69 (1987) 163–174.

[68] C. F. Karney, Fokker-planck and quasilinear codes, Computer Physics Reports 4 (1986) 183–244.

[69] C. Buet, S. Cordier, Conservative and entropy decaying numerical scheme for the isotropic fokker–planck–landau equation, Journal of Computational Physics 145 (1998) 228–245.

[70] L. Pareschi, G. Russo, Numerical solution of the boltzmann equation i: Spectrally accurate approximation of the collision operator, SIAM journal on numerical analysis 37 (2000) 1217–1245.

[71] S. Jin, L. Wang, An asymptotic preserving scheme for the vlasov-poisson-fokker-planck system in the high field regime, Acta Mathematica Scientia 31 (2011) 2219–2232.

[72] S. Jin, Y. Zhu, E. Zuazua, The vlasov–fokker–planck equation with high dimensional parametric forcing term, Numerische Mathematik 150 (2022) 479–519.

[73] J. Y. Lee, J. W. Jang, H. J. Hwang, The model reduction of the vlasov–poisson–fokker–planck system to the poisson–nernst–planck system via the deep neural network approach, ESAIM: Mathematical Modelling and Numerical Analysis 55 (2021) 1803–1846.

[74] R. Berger, J. Albritton, C. Randall, E. Williams, W. Kruer, A. Langdon, C. Hanna, Stopping and thermalization of interpenetrating plasma streams, Physics of Fluids B: Plasma Physics 3 (1991) 3–12.

[75] D. Ghosh, T. D. Chapman, R. L. Berger, A. Dimits, J. Banks, A multispecies, multifluid model for laser–induced counterstreaming plasma simulations, Computers & Fluids 186 (2019) 38–57.

[76] P. Rambo, J. Denavit, Interpenetration and ion separation in colliding plasmas, Physics of Plasmas 1 (1994) 4050–4060.

[77] P. Rambo, R. Procassini, A comparison of kinetic and multifluid simulations of laser-produced colliding plasmas, Physics of Plasmas 2

(1995) 3130–3145.
[78] E. Sonnendrücker, F. Filbet, A. Friedman, E. Oudet, J.-L. Vay, Vlasov simulations of beams with a moving grid, Computer Physics Communications 164 (2004) 390–395.